

63-3-2

①

401 395

**MATERIAL PROCESSING AND PHENOMENA INVESTIGATIONS
FOR FUNCTIONAL ELECTRONIC BLOCKS**

S. J. Angello, Project Leader

SECOND INTERIM ENGINEERING REPORT

Contract No. AF 33(657)-9897

(1 January through 6 March 1963)

Prepared for



**Electronics Technology Laboratory
Aeronautical Systems Division
United States Air Force
Wright-Patterson Air Force Base, Ohio**



**WESTINGHOUSE RESEARCH LABORATORIES
PITTSBURGH • PENNSYLVANIA**

\$6.60

④ \$6.60
⑤ 744 500

⑥ MATERIAL PROCESSING AND PHENOMENA INVESTIGATIONS
FOR FUNCTIONAL ELECTRONIC BLOCKS

⑧ S. J. Angello, Project Leader
⑨ 6 Mar 63
⑩ 61p. incl. illus. tables
⑪ NA

⑦ SECOND INTERIM ENGINEERING REPORT

⑫ Contract No. AF 33(657)-9897
⑬ NA

✓ (1 Jan ~~1963~~ through 6 Mar ~~1963~~)

Prepared for

Electronics Technology Laboratory
Aeronautical Systems Division
United States Air Force
Wright-Patterson Air Force Base, Ohio

AB

TABLE OF CONTENTS

| | <u>Page</u> |
|---|-------------|
| <u>SUMMARY</u> | 1 |
| <u>PROBLEMS AND GENERAL DISCUSSION</u> | |
| <u>A. Electrochemical Techniques</u> | |
| A.1. Geometry Control and Anodic Oxide Growth on N-type Silicon | 3 |
| A.1.1. Evaluation of Electrolytes | 3 |
| A.1.2. Evaluation of Silicon Crystals | 7 |
| A.2. Measurements of Surface Recombination Velocity as a Function of Impurities Incorporated into Anodic Oxide Films | 9 |
| A.3. Preparation of High Resistivity N-type Layers by Diffusion of Phosphorous from Very Thin or Very Weakly Doped Anodic Oxide Films | 10 |
| A.4. Measurement of Out-Diffusion of Phosphorous from Doped Anodic Oxide Films | 15 |
| A.5. Surface Preparation | 17 |
| <u>B. Electron Beam Techniques</u> | |
| B.1. Refinement of Instrument Performance | 18 |
| B.2. Scanning Electron Microscopy | 20 |
| B.3. Electron Beam Fabricating Techniques | 31 |
| B.4. Electron Beam Exposure of Resist Films | 36 |
| B.4.1. Uniform Film Thicknesses | 36 |
| B.4.2. Types of Organic Resists | 42 |
| B.4.3. Problems in Using Resist Films | 44 |
| B.4.4. Exposure Studies | 48 |
| <u>C. Laser Techniques</u> | |
| C.1. Laser Bonding Gold Leads to Aluminum Coated Silicon | 53 |
| C.2. Laser Bonding Gold Leads to Alloy Junction Diodes | 57 |
| C.3. Laser Equipment - Neodymium Doped Glass Laser Rods | 57 |

LIST OF TABLES AND FIGURES

TABLES

| | <u>Page</u> |
|---|-------------|
| Table I - Dry Film Thickness (KMER) | 42 |
| Table II - Tensile/Shear Bond Strengths | 60 |

FIGURES

| | |
|--|----|
| Fig. 1 - Voltage-time curve for anodization of 2 ohm-cm ² p-type silicon at a constant current of 3 ma/cm ² in a solution of 2% NaNO ₂ in tetrahydrofurfuryl alcohol. | 5 |
| Fig. 2 - Current decay at constant voltage of 50 v for a 31 ohm-cm n-type silicon web under illumination. Electrolyte: 2% NaNO ₂ in THF. | 6 |
| Fig. 3 - Blocking of the anodic current by 31 ohm-cm n-type silicon web in darkness. Comparison between bare surface and previous anodization to 50 volts in light. | 8 |
| Fig. 4 - Response of n-type silicon photodiode (thickness about 20 mils) relative to a detector of known sensitivity for various penetration depths of the incident radiation. Front surface of the silicon in contact with air. | 11 |
| Fig. 5 - Typical photoresponse _n - cell bias curve for silicon photodiode (same as Fig. 4) in contact with an electrolyte (1% Na ₂ SO ₄ in water). | 12 |
| Fig. 6 - Ultraviolet absorption of commercial grade 85% orthophosphoric acid; two different lots from the same supplier. | 14 |
| Fig. 7 - Ultraviolet absorption of pyrophosphoric acid, prepared by dehydration of orthophosphoric acid. Absorption curve for starting material is also shown. | 16 |
| Fig. 8 - Power transistor section of WM1105 functional electronic block (scanning electron micrograph). | 21 |
| Fig. 9 - Power transistor section of WM1105 functional electronic block (scanning electron micrograph). | 22 |
| Fig. 10 - Power transistor section of WM1105 functional electronic block (scanning electron micrograph). | 24 |

LIST OF TABLES AND FIGURES
(continued)

| <u>FIGURES</u> | <u>Page</u> |
|---|-------------|
| Fig. 11 - Power transistor section of WM1105 functional electronic block (scanning electron micrograph). | 26 |
| Fig. 12 - The geometry of the Device (Field-effect transistor). | 29 |
| Fig. 13 - Scanning electron micrographs of a pair of silicon field-effect devices. | 30 |
| Fig. 14 - Scanning electron micrographs of glass test plate with copper spot pattern partially coated with aluminum film. Entire plate coated with Kodak Photoresist layer. | 33 |
| Fig. 15 - Scanning electron micrographs of a silicon field-effect device under various bias conditions. | 35 |
| Fig. 16 - Effect of scattering on resist film exposure. | 37 |
| Fig. 17 - Variation of Kodak Photoresist thickness with angular velocity. | 38 |
| Fig. 18 - Variation of Kodak Metal Etch Resist thickness with angular velocity. | 39 |
| Fig. 19 - Intercepts of KMER dilution curves vs. dilution ratio. | 41 |
| Fig. 20 - Coving with negative-acting and positive-acting resists. | 45 |
| Fig. 21 - Interference fringe pattern and cross-section of resist stripe. | 47 |
| Fig. 22 - Normalized KPR thickness vs. light exposure value. | 49 |
| Fig. 23 - Normalized KPR thickness vs. electron exposure value for 4 electron accelerating voltages. | 50 |
| Fig. 24 - Normalized KPR thickness vs. electron exposure value for 4 electron accelerating voltages. | 51 |
| Fig. 25 - Metallographic section of Sample L-7, two mil gold wire laser bonded to silicon substrate. | 55 |

LIST OF TABLES AND FIGURES
(continued)

FIGURES

Page

- | | |
|---|----|
| Fig. 26 - Metallographic section of Sample L-8, two mil gold wire laser bonded to silicon substrate. | 55 |
| Fig. 27 - Metallographic section of Sample L-10, two mil gold wire laser bonded to silicon substrate. | 56 |
| Fig. 28 - Sketch of thermocompression bonded and laser bonded leads before and after bending, prior to testing. | 58 |
| Fig. 29 - Tensile/Shear strength test, sketch of arrangement. | 59 |

5 April 1963

MATERIAL PROCESSING AND PHENOMENA INVESTIGATIONS
FOR FUNCTIONAL ELECTRONIC BLOCKS

* * * * *

SECOND INTERIM ENGINEERING REPORT

Contract No.

AF 33(657)-9897

Period Covered

1 January through 6 March 1963

SUMMARYA. Electrochemical Techniques

Evaluation of electrolytes, and of n-type silicon as a function of resistivity and type of crystal, has been carried out for the purpose of geometry control over anodic oxide growth. A solution of sodium nitrite in tetrahydrofurfuryl alcohol was found to enable blocking of the anodic current in darkness up to 300 volts, and for periods up to an hour, on higher resistivity silicon. Under illumination a non-doped oxide film of high quality can be grown in the same electrolyte.

On 100 ohm-cm n-type silicon (float zoned material), the anodic current in darkness remains blocked both on the bare and on the previously anodized surface. On 25 ohms-cm n-type silicon (float zoned material), blocking of the anodic current on a previously anodized surface is difficult beyond about 75 volts. 31 ohm-cm n-type silicon web, however, blocked the anodic current even on a previously anodized surface up to 175 volts.

The opto-electrochemical system for investigation of the surface recombination velocity of n-type silicon as a function of impurities incorporated into the anodic oxide film is being checked out. Difficulties are being encountered with the bridge circuit.

The method of preparation of pyrophosphoric acid is being standardized as a preliminary step for investigating the reproducibility of high resistivity n-type layers prepared by diffusion of phosphorous from doped anodic oxide films.

The oxygen pressure required to stabilize phosphorous-doped anodic oxide films in vacuo at 1175°C has been found to be 0.025 ± 0.005

Torr for heavily doped films. The less phosphorous, the smaller the necessary oxygen pressure.

A new lapping and polishing machine, invented at Westinghouse, has been adapted for the polishing of large silicon bars. This will save much time previously spent on surface preparation.

B. Electron Beam Techniques

Modifications have been made during this period which have greatly improved the performance of the Westinghouse high resolution scanning electron beam instrument. Resolutions of better than 0.5 micron have been achieved in the electron spot size. The accuracy of positioning a specimen in the instrument has been markedly improved by modifications to the mechanical stage in the specimen chamber.

Scanning electron micrographs have been made of p-n junctions on silicon devices under various bias conditions. The junctions are clearly visible, even when the surface of the device is coated with a passivating layer of silicon dioxide several thousand Angstrom units thick. In fact, such passivated junctions can even be located beneath a one micron layer of evaporated aluminum.

Techniques have been worked out for obtaining satisfactory registration of the workpiece in the instrument during various semiconductor device process steps, such as the exposure of a photoresist layer for the purpose of putting down a gate electrode very accurately on a field-effect transistor.

C. Laser Techniques

Metallographic cross-sections of the joint region where 0.002" gold wires were attached to an aluminum coated silicon substrate, using laser techniques with the Trion LS-2 ruby system, reveal negligible thermal damage. Initial tests of the tensile and shear strength of such lasered bonds indicate satisfactory adhesion. Leads can be attached to previously fabricated silicon junction diodes without changing any of their electrical characteristics.

A neodymium-doped glass rod has been received and tested. The energy output of this laser rod has proven to be well below that of similar rods obtained from the same supplier.

PROBLEMS AND GENERAL DISCUSSION

A. Electrochemical Techniques

A.1. Geometry Control of Anodic Oxide Growth on N-type Silicon

A.1.1. Evaluation of Electrolytes

An acceptable electrolyte must satisfy several criteria: in darkness it should pass only a very small leakage current up to very high applied voltages, under illumination it should permit the growth of high quality anodic oxide films; it should not have too high a resistivity, which would cause large IR drops in the solution; it should, preferably, not be too viscous or hygroscopic; and finally, no carbon must get incorporated into the oxide from the organic solvent during anodization, otherwise the oxide would deteriorate during heat treatment due to volatilization of CO_2 or CO .

It has been found that a solution of sodium nitrite in tetrahydrofurfuryl alcohol appears to meet all of these requirements; the concentration of the nitrite is apparently not critical. On both 25 and 100 ohm-cm n-type silicon (float-zones material) dark blocking up to 300 volts for over 40 minutes has been observed.

It is, however, anticipated that an "edge problem" will be encountered in actual geometry control work. It cannot be expected that the edge of an anodic oxide film growing under local illumination will be completely abrupt; rather, a sloping down from the full oxide height to the bare silicon surface over very small dimensions must be expected. In this case it will not be the dark blocking power of the

bare silicon surface, but the dark blocking power of a slightly oxidized silicon surface which determines the quality of pattern reproduction by the oxide.

For this reason the dark blocking ability of 25 and 100 ohm-cm n-type silicon has been tested, the silicon having been previously anodized under illumination to 50 volts, and then put into darkness while applying a high anodic bias. The 100 ohm-cm material passes this test without difficulty, but on 25 ohm-cm material it is difficult to exceed 75 volts (dark blocking) under these circumstances. However, 75 volt films are quite sufficient for many device applications presently being considered. We are therefore optimistic that no serious difficulties have to be solved in this area.

Evaluation of the forming properties of an electrolyte is best done on p-type material where there are no complications due to lack of holes. Figure 1 shows the rise of potential with time during the anodization of 2 ohm-cm p-type silicon (float zoned material) in a solution of 2% NaNO_2 in tetrahydrofurfuryl alcohol. The reason for the sudden change in the slope at about 40 volts is as yet unexplained. It signifies an increase in current efficiency. Even so, the current efficiency on the steeper portion of the curve is only about 1%, the rest of the current going into an electrode reaction other than oxide formation.

Figure 2 shows the decay of the anodic leakage current with time for a 31 ohm-cm n-type silicon web formed to 50 volts, and then kept at a constant voltage of 50 volts. It can be seen that for times

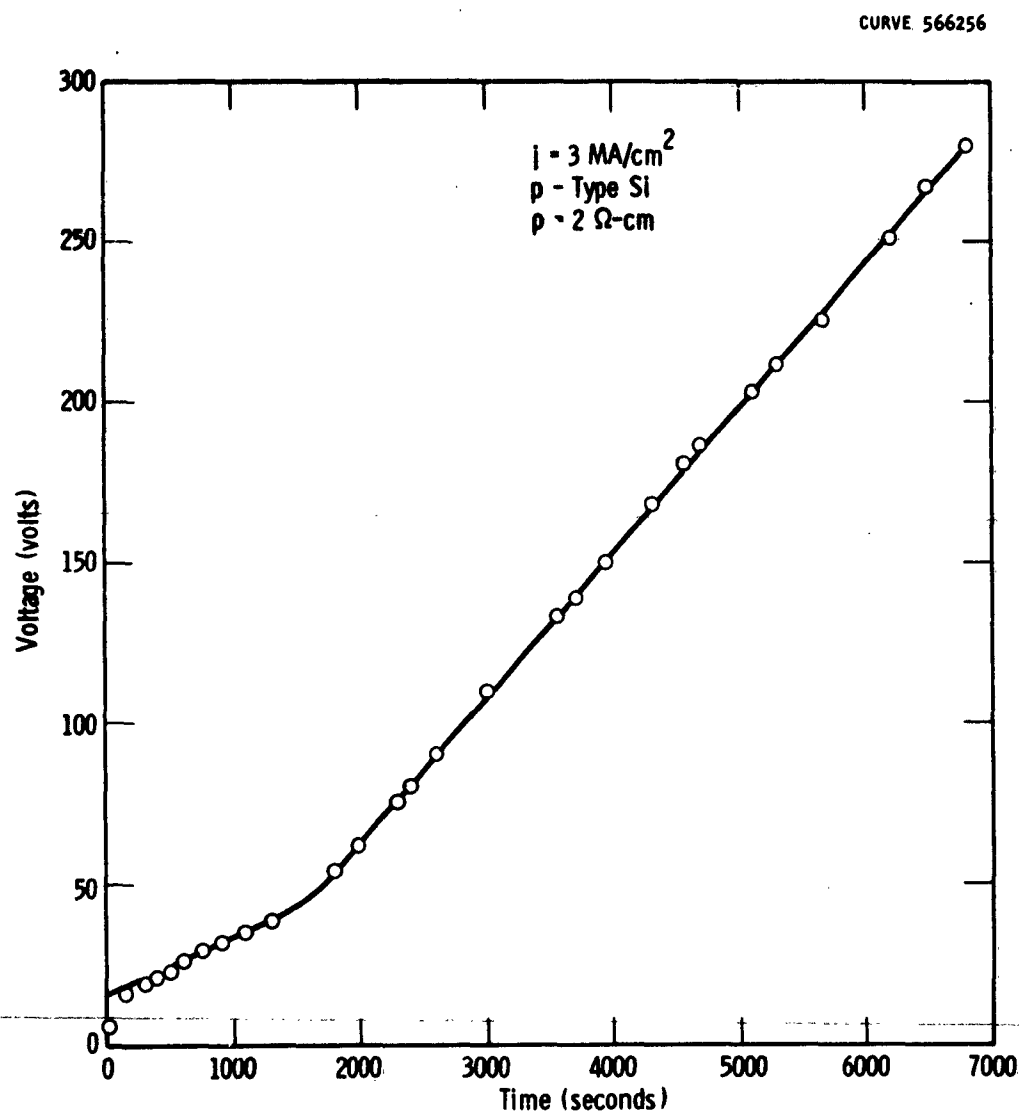


Fig. 1—Voltage-time curve for anodization of 2 ohm-cm p-type silicon at a constant current of 3 ma/cm² in a solution of 2% NaNO₂ in Tetrahydrofurfurylalcohol.

CURVE 566257

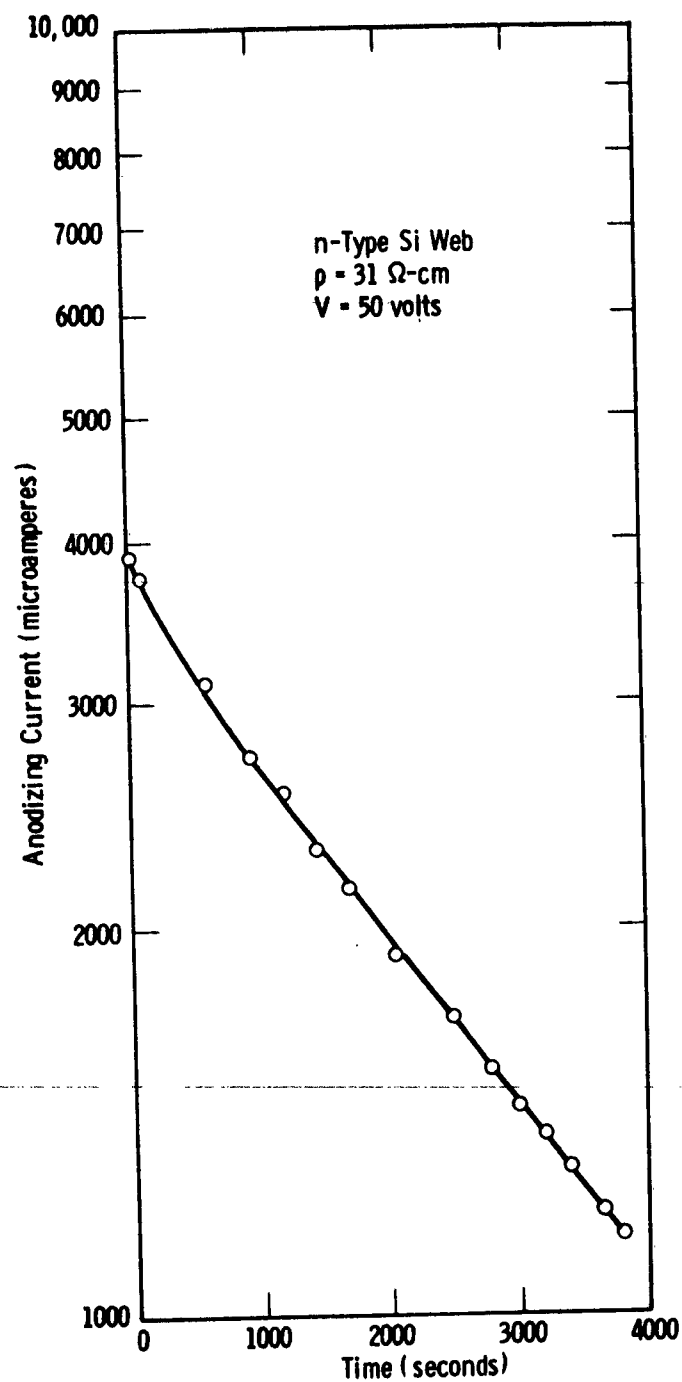


Fig. 2—Current decay at constant voltage of 50 v for a 31 ohm-cm n-type silicon web under illumination. Electrolyte: 2% NaNO_2 in THF.

longer than about 400 seconds the semilog plot gives a straight line relationship. The slight deviation from linearity at short times is probably due to a contribution by the ionic current.

Figure 3 gives the leakage current of a 31 ohm-cm n-type silicon web as a function of applied bias in complete darkness for two different surface conditions. The bare silicon surface yields a completely linear plot, whereas the same sample after previous anodization under illumination to 50 volts exhibits a rise of current with applied voltage which has a considerably greater slope. Even so, the absolute amount of leakage current is quite small, particularly considering that most of it is electronic (i.e. not contributing to the oxide growth).

A.1.2. Evaluation of Silicon Crystals

From a practical point of view, i.e. suitability for a continuous commercial operation, silicon webs appear much more attractive for geometry control of anodic oxide films than do silicon discs. The following reason is as follows: a light pattern can be either focused onto the silicon surface undergoing anodization, in which case the light must penetrate the layer of liquid without suffering a distortion of the image; or, if the silicon crystal is sufficiently thin, the light pattern could be focused on the dry back face of the crystal, obviating all optical problems in the electrolyte. Silicon webs can be made as thin as a few mils. They also form a natural trough (i.e. when held horizontally the anodizing solution can be confined to the upper surface of the web). Provided a sufficiently

CURVE 566258

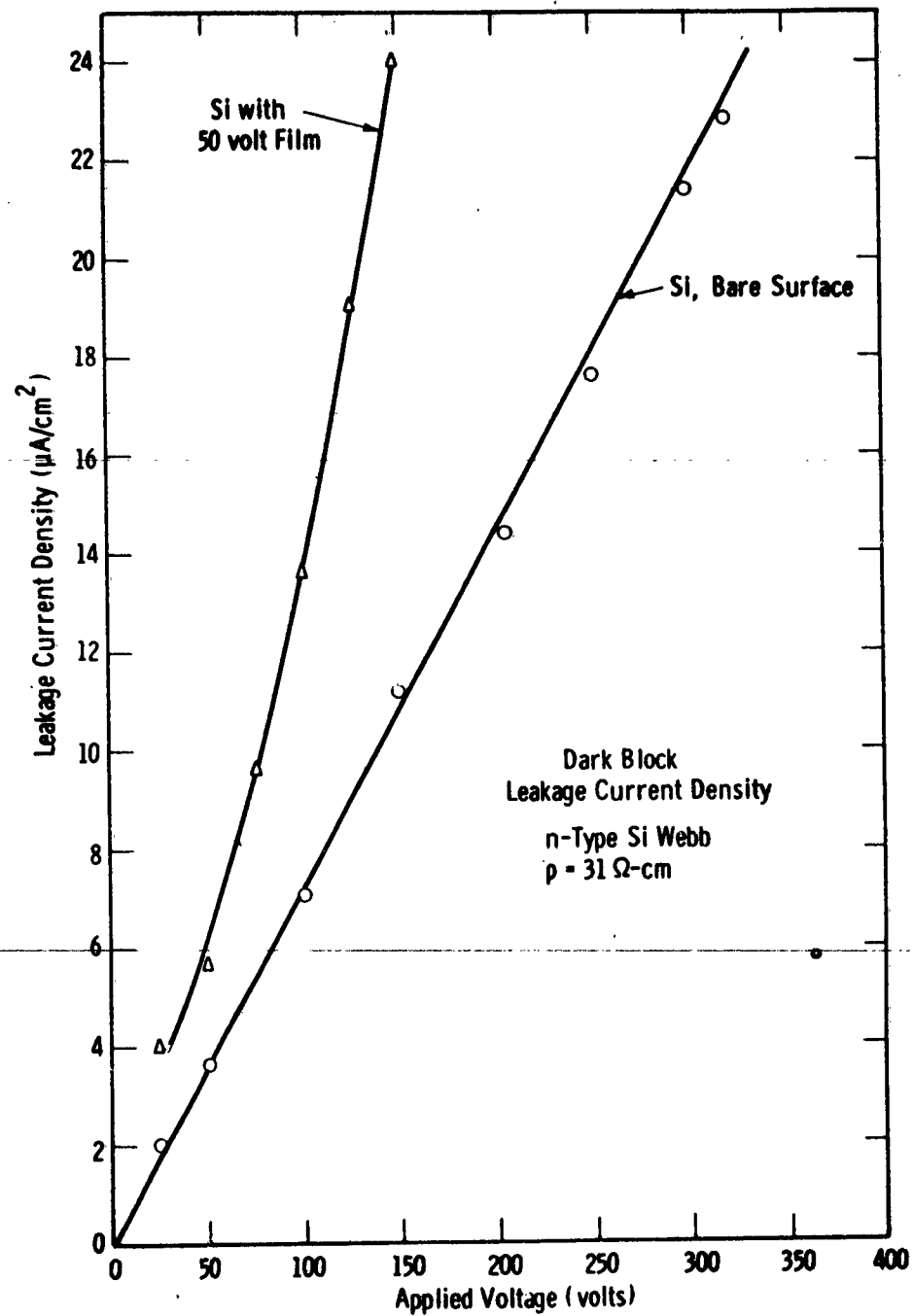


Fig. 3—Blocking of the anodic current by 31 ohm-cm n-type silicon web in darkness. Comparison between bare surface and previous anodization to 50 volts in light.

high reverse bias is applied between the solution and the silicon, the space charge region in the semiconductor at the silicon-solution interface will be spread through the whole thickness of the web, and minority carriers generated optically at the back surface will be swept by the field to the front surface with little or no sidewise diffusion. We have shown earlier that this situation can be realized.

Various n-type silicon webs which were not grown specifically for our purpose have been tested by us in the past. These webs, of nominal resistivity in the 20 to 100 ohm-cm range, had proved unsatisfactory, since they apparently contained regions of varying (or even opposite type) doping level. The segregation coefficients of the commonly used dopants are such that during growth of high resistivity n-type silicon webs there is a tendency for p-type islands to develop.

We have now obtained 31 ohm-cm n-type silicon web from the Youngwood Semiconductor Division which appears to be of uniform resistivity throughout. This web blocks the anodic current in darkness up to 320 volts, and up to 175 volts after previous anodization in light to 50 volts. (See Fig. 3)

A.2. Measurements of Surface Recombination Velocity on Silicon as a Function of Impurities Incorporated into Anodic Oxide Films

The addition of a few more auxiliary optical filters to our collection has enabled the photoresponse of a silicon photodiode immersed in an electrolyte solution to be measured at twenty-three different wavelengths. Minority carriers generated by the light incident from the solution side

will diffuse to the p-n junction; the shorter the generating wavelength (i.e. the closer to the surface the carriers are being generated), the more pronounced the effect of surface recombination velocity in annihilating these excess minority carriers before they can reach the p-n junction. The surface recombination velocity can be varied by applying a bias to the silicon surface by means of an auxiliary platinum electrode in the solution. The purpose of the investigation is to study in detail the effect on the surface recombination velocity of impurities incorporated into the oxide. That such an effect exists is known from the disappearance of dark blocking on n-type silicon when anodized in phosphate- or arsenate-containing solutions.

Smooth curves of the expected form have been obtained on dry silicon photodiodes, as a function of penetration depth of the light, as shown in Fig. 4. On a silicon surface in contact with an electrolyte, the surface recombination velocity can be varied by applying bias. This effect is shown in Fig. 5. However, here a complication arises: not only the p-n junction of the photodiode, but also the space charge region at the electrolyte interface generates a photovoltage. A circuit is being designed to differentiate between these two signals.

A.3. Preparation of High Resistivity N-Type Layers by Diffusion of Phosphorous from Very Thin or Very Weakly Doped Anodic Oxide Films

It is obvious that this aim can be achieved in principle. What is required is to make the method at least as reproducible as techniques currently in industrial use, which employ diffusion from the gas phase. Precise control of the amount of phosphorous incorporated into the oxide during anodization is therefore a prerequisite of success.

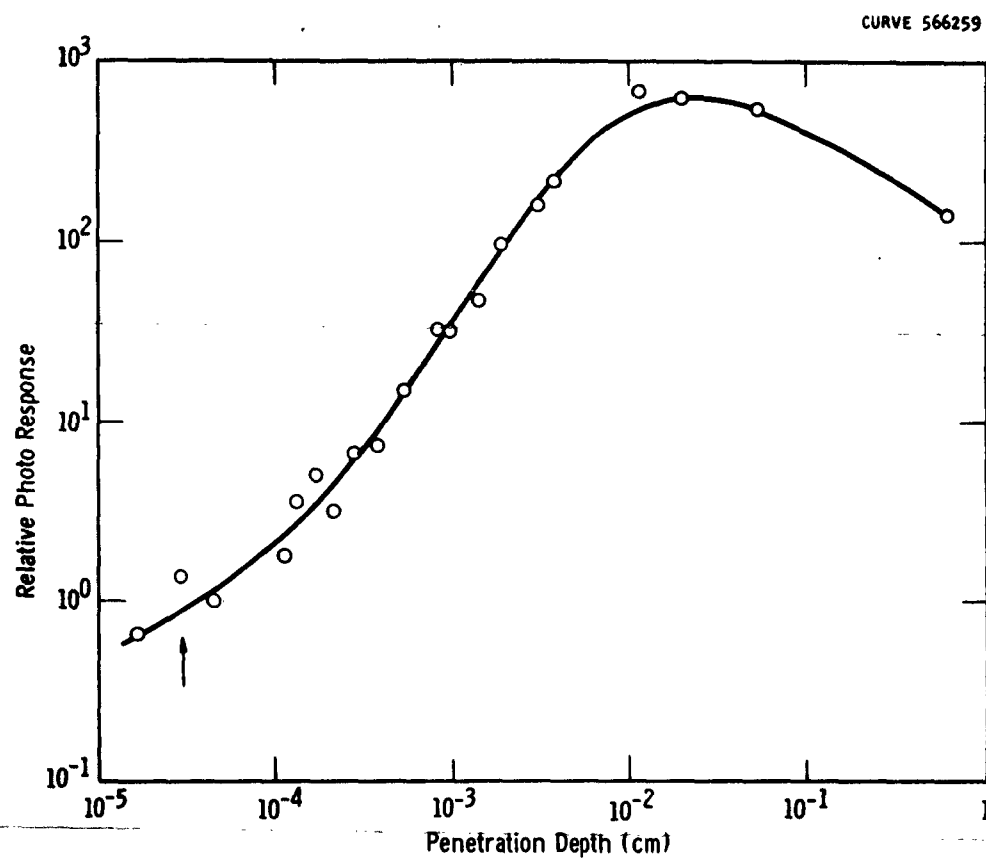


Fig. 4—Response of n-type silicon photodiode (thickness about 20 mils) relative to a detector of known sensitivity for various penetration depths of the incident radiation. Front surface of the silicon in contact with air.

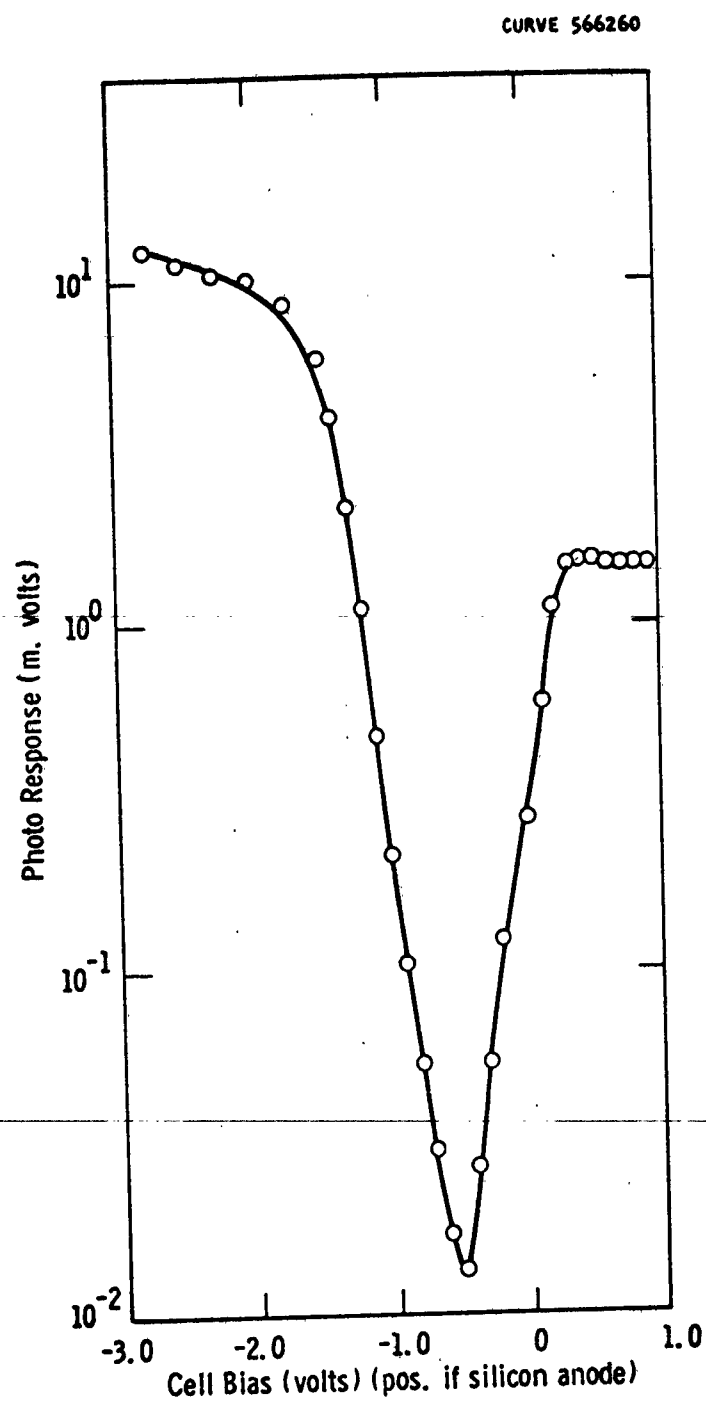


Fig. 5- Typical photoresponse - cell bias curve for silicon photodiode (same as Fig. 4) in contact with an electrolyte (1% Na_2SO_4 in water).

Two methods of preparing pyrophosphoric acid of the desired $P_2O_5:H_2O$ ratio* are feasible: dehydration of analytical grade orthophosphoric acid by heating to approximately $300^{\circ}C$ in a quartz vessel; or by reaction of analytical grade P_2O_5 with the required amount of water. Both methods have their drawbacks: reaction of large amounts of P_2O_5 with water is not a harmless operation, whereas commercially available analytical grade orthophosphoric acid, according to findings at Siemens-Schuckert, may be contaminated with enough sulphur to change the diffusion profile. (Sulphur has a very high diffusion coefficient in silicon.) We shall definitely have to settle for the P_2O_5 method if the contamination with sulphur also applies to analytical grade orthophosphoric acid as currently available in the United States.

Even if P_2O_5 and water are mixed in the right proportions it will still be necessary to heat the mixture in order to establish equilibrium of the various acids. (See footnote.) Loss of water must obviously be avoided during this operation.

The most sensitive method of controlling the composition of the pyrophosphoric acid appears to be by means of the ultraviolet spectrums. Pyrophosphoric acid has a strong absorption band centered at 2325 AU, peak width about 100 AU, whereas the absorption by orthophosphoric acid in this region is much weaker. (See Fig. 6.) It has been found that the degree

* What is called "pyrophosphoric acid" (i.e. $H_4P_2O_7$), is in reality a mixture of various acids - ortho, pyro, meta, and polymers thereof, corresponding to the overall formula $H_4P_2O_7$. Salts of the pyrophosphoric acid, however, are well known, and correspond to the formula $Me_4P_2O_7$.

CURVE 566261

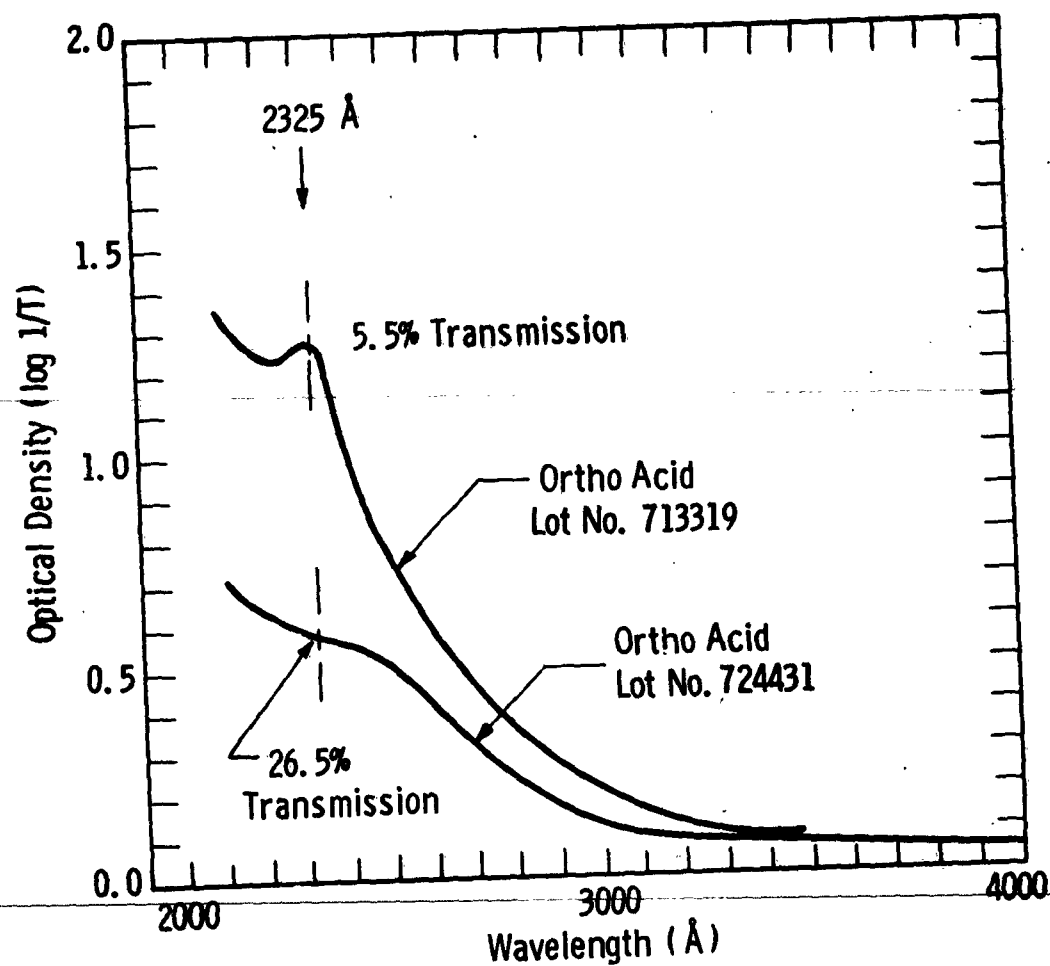


Fig. 6—Ultraviolet absorption of commercial grade 85% orthophosphoric acid; two different lots from the same supplier

of dehydration of the orthophosphoric acid by heating to 300°C depends not only on the highest temperature reached during dehydration, but also on the period of time kept at or near the peak temperature. In other words, the loss of water is a slow process.

It is planned to set up a system that can monitor the absorption spectrum, during the dehydration or homogenization process. It has also been found, as can be seen from Fig. 7, that the absorption spectrum of two different batches of analytical grade orthophosphoric acid (from the same supplier) was markedly different. We do not know, as yet, whether this difference also shows up in the final composition.

A.4. Measurement of Out-Diffusion of Phosphorous from Doped Anodic Oxide Films

It has been shown that an absolute pressure of 0.025 ± 0.005 mm Hg of oxygen is required to prevent gross deterioration of the phosphorous doped anodic oxide films grown on silicon when the sample temperature is held at 1170°C for $1\frac{1}{2}$ to 2 hours. The required pressure is probably dependent on the phosphorous content of the oxide (above case $\sim 10\% \text{P}_2\text{O}_5$), since films containing no phosphorous (grown from NaNO_2 solutions) did not deteriorate even at pressures of 0.01 mm Hg of oxygen. The above pressure (0.025 mm Hg) is low enough (mean free paths ~ 1 cm) to expect success from an experiment designed to collect on a nearby cold foil any phosphorous diffusion out of the oxide film. Using radioactive phosphorous the rate of out-diffusion can thus be measured by counting the activity accumulating on the foil.

CURVE 566262

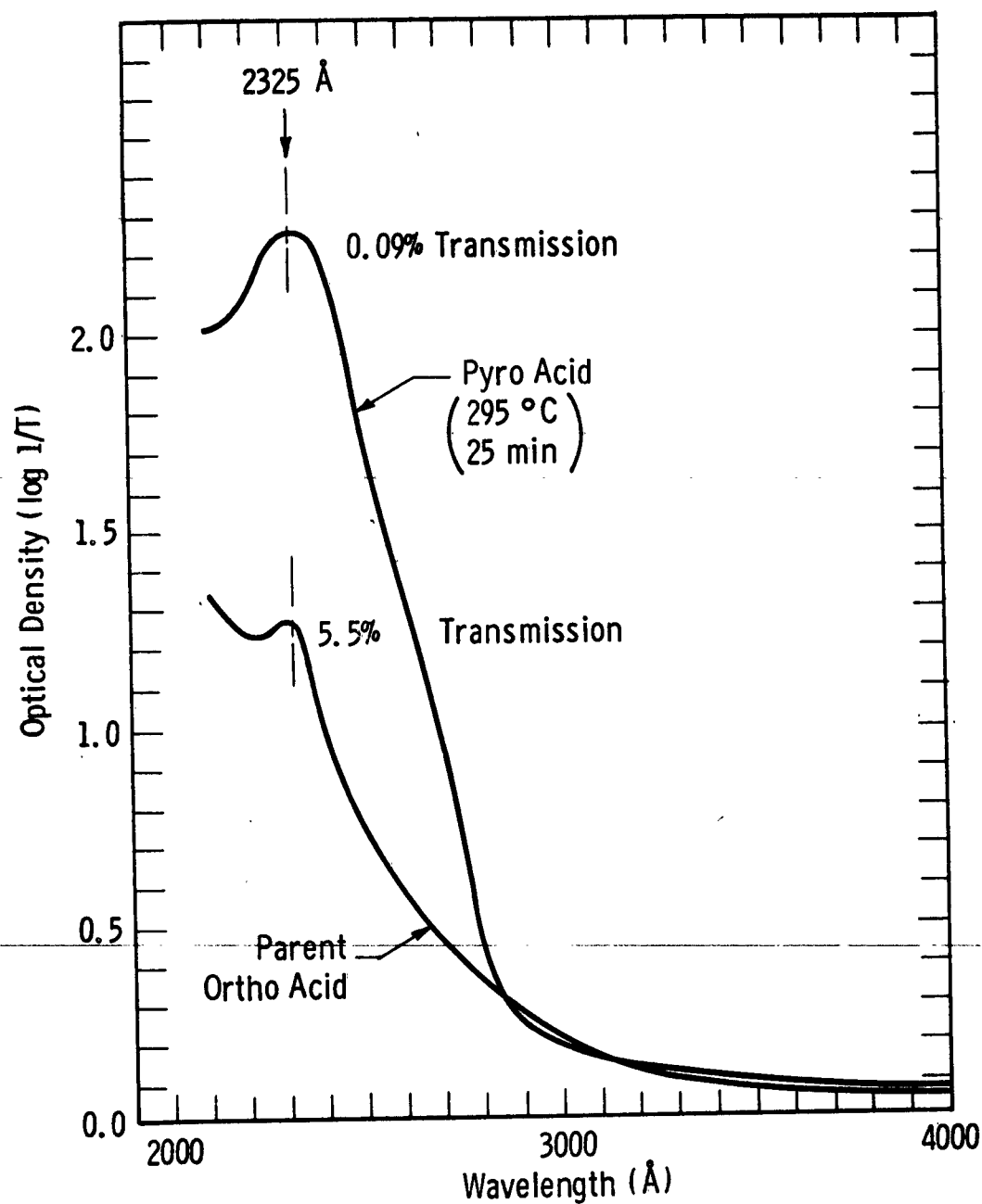


Fig. 7—Ultraviolet absorption of pyrophosphoric acid, prepared by dehydration of orthophosphoric acid. Absorption curve for starting material is also shown.

An alternative approach to the out-diffusion measurement is being investigated. It involves heating phosphorous-doped oxide-coated silicon samples quickly to the diffusion temperature (1170°C), maintaining this temperature for various lengths of time for different samples, and then cooling quickly. By measurements of the activity remaining on or in the samples, the amount and rate of out-diffusion can be calculated.

A.5. Surface Preparation

A newly developed lapping and polishing machine has been adapted for the polishing of large silicon bars. Polishing operations using wheels and hand polishing have consumed much time in the past.

Silicon bars are more economical for electrochemical work followed by diffusion than are discs. A single bar will provide the substrate for about eight separate experiments, whereas discs are consumed in a single run. However, the surfaces of the bars must be as good as those of highly polished discs, especially for tracer work, where the surface roughness factor is quite important. It was found that large areas of this configuration ($2\frac{1}{2}$ " by $\frac{1}{4}$ ") are difficult to polish. The problem has, however, been solved by appropriate procedures, and we expect to save much time, which in the past was spent on surface preparation.

B. Electron Beam Techniques

B.1. Refinement of Instrument Performance

This work area involves principally (i) the refinement of the electron optics and associated circuitry to give electron beams of 0.1 micron diameter for high resolution photoengraving techniques, and (ii) the completion and perfection of the pattern scanning and registration features of the instrument. These are essential for the fabrication of the complex, superimposed patterns typically encountered on functional electronic blocks.

The following major tasks have been accomplished:

(i) A beam intensity between 0.5 and 1.0 times the theoretical value has been obtained with a 50 micron aperture at the crossover. This well-defined, round source is ideal for scanning microscopy.

However, for some applications, when the beam voltage must be varied often over the 5 kv to 50 kv range, the aperture is inconvenient, since the anode height must be altered to obtain optimum brightness. In these applications, the aperture is not used, and the source is the electron gun crossover.

(ii) A newly designed stigmator has been used to replace the commercial version used previously. The beam current available for a given spot size on the specimen has been increased approximately sixteen times by this modification.

(iii) Magnetic screening of the specimen chamber has been greatly improved. This has made voltage contrast easily obtainable.

(iv) A new pole-piece for the final lens was installed, reducing the spherical aberration of the final lens from 360 cm to an estimated 4 cm, and also greatly reducing the magnetic field at the specimen.

The Canalco lens without a pole-piece has low spherical aberration, but has large fringing magnetic fields which impair secondary electron collection and the contrast due to surface potential variations on the specimen.

(v) Scintillator buttons in the collector have been aluminized more efficiently, resulting in a four-fold increase in the original signal-to-noise ratio. A Zener diode across the first stage of the photomultiplier keeps the gain of the stage optimized, regardless of the overall photomultiplier gain, and thus optimizes the signal-to-noise ratio of the video signal.

(vi) A new cathode ray tube, with a long persistence P-7 phosphor has been installed. Visual examination of the specimen at a much higher signal-to-noise ratio is now possible, as the long persistence of the phosphor integrates out much of the beam shot noise previously present.

(vii) Problems associated with drift in the direct-coupled video amplifier have been greatly reduced by circuit modifications within the amplifier.

(viii) Discovery and replacement of a defective traverse rod has resulted in a marked improvement in the accuracy of the mechanical stage in the specimen chamber. Positional accuracy of the specimen (as traversed mechanically) is now better than 0.0005" over the entire one inch square traverse area.

(ix) An improved motor drive has been installed to traverse the mechanical stage for the purpose of bombarding stripes on a specimen with the electron beam.

(x) A 35 mm camera has been fitted to the viewing kinescope of the scanning electron microscope in order to obtain higher quality micrographs (at lower cost) than is possible with the Polaroid camera previously used.

B.2. Scanning Electron Microscopy¹

The variations and distribution of electrical potentials on the surface of a functional electronic block (FEB) Type WM1105 have been observed during the past quarter. Figure 8 shows low magnification micrographs of the audio power transistor section. With no bias applied, the surface appears as shown in Fig. 8(a); the emitter-base junction, under reverse bias, is shown in Fig. 8(b); the base-collector junction, with reverse bias applied, is shown in Fig. 8(c). Figure 8(d) is an optical micrograph of the same transistor, shown for comparison.

The surface of this device was passivated with a thermally grown layer of silicon dioxide a few thousand Angstrom units thick. The potential difference between adjacent areas is clearly visible as a shift in brightness. Even though the surface of the device, due to the silicon dioxide layer, is an insulator, there is no evidence of instability or charging. In addition, the surface potential of the silicon dioxide varies as the potential of the semiconductor directly beneath it.

The emitter-base junction of this device was studied at higher magnification, as shown in Fig. 9. A lead is connected to the emitter region

1. See First Interim Engineering Report, AF 33(657)-9897, "Material Processing and Phenomena Investigations for Functional Electronic Blocks", Westinghouse Research Laboratories, January 10, 1963, pp 29-38.



(a) No applied bias



(b) Emitter-base junction
reverse-bias = 6 v.



(c) Base-collector junction
reverse-bias = 6 v.



(d) Light micrograph
M = 50 x

Fig. 8. Power transistor section of WM1105
functional electronic block



(a) No applied bias



(b) Emitter-base junction
reverse-bias = 1 v.



(c) Emitter-base junction
reverse-bias = 2 v.



(d) Emitter-base junction
reverse-bias = 3 v.

Fig. 9 Power transistor section of WML105
functional electronic block

which has a layer of aluminum alloyed to the semiconductor. The base region (shown on the left) is also covered with a layer of aluminum. Various imperfections, in the form of pits and fine lines, are visible on the aluminum surface. The actual junction is located under a silicon dioxide passivation layer, which changes height approximately midway between the emitter and base aluminum coatings. The photoresist masking appears to have been scratched during the processing of this device, resulting in the scratch which is apparent at the emitter-base junction. A much thinner oxide layer covers the base side of the junction where this scratch occurred, but no degradation of the performance of the unit resulted.

This series of micrographs shows clearly that emitter-base potentials of one volt are easily detected, and that relative changes of one volt (e.g. from two volts to three volts) are also easily detected. Visual quality control of this device, using an optical microscope, might lead to its rejection, because of the obvious scratch in the passivating oxide. Scanning electron micrographs reveal that this flaw has not affected the location of the junction, or the distribution of potentials under bias. When the information from the scanning electron microscope is fed back into the device processing operation, improvements in processing, and ultimate device reliability seem sure to result.

Similar micrographs of the base-collector junction of the power transistor on FEB Type WM1105 were obtained and are shown in Fig. 10. For comparison the oxide was removed by etching the structure with pure hydrofluoric acid. The device was then rinsed in deionized water and methanol. The micrographs shown in Figs. 10(c) and 10(d) were then obtained. Comparing Figs. 10(a) and 10(c), note the step variation in oxide thickness, visible



(a) No applied bias



(b) Base-collector junction
reverse-bias = 4 v.



(c) SiO_2 passivation removed.
No applied bias



(d) SiO_2 passivation removed.
Base-collector junction
reverse bias = 4 v.

Fig. 10 Power transistor section of WM1105
functional electronic block

in Fig. 10(a), has disappeared in Fig. 10(c), and that a circular imperfection on the silicon surface has appeared. In Fig. 10(c), the junction position is barely visible at the top of the base region, and is not apparent at the left of the picture. When the bias is applied to the stripped junction, as in Fig. 10(d), the base boundary becomes clearly visible, and, within experimental error, is in the same position as determined in Fig. 10(b), through the oxide layer.

A similar set of micrographs were obtained at the emitter-base junction, as shown in Fig. 11. The thicker silicon dioxide layer over this junction appears darker under zero bias conditions. The contrast between opposite sides of the junction changes dramatically when bias is applied, as can be seen when comparing Figs. 11(a), 11(b), and 11(c). Figure 11(d) shows this same region again, however with the passivating oxide layer removed. This particular micrograph is much noisier than the others, because the relative secondary emission of bare silicon is much lower than that of silicon coated with silicon dioxide. Thus, this work has shown not only that it is possible to obtain clear contrast across a p-n junction under a silicon dioxide layer, but that the silicon dioxide layer indeed appears to be helpful with respect to signal to noise ratio.

The above micrographs are representative of over 150 pictures taken during the past quarter. Based on the information obtained from this work, it can be stated that:

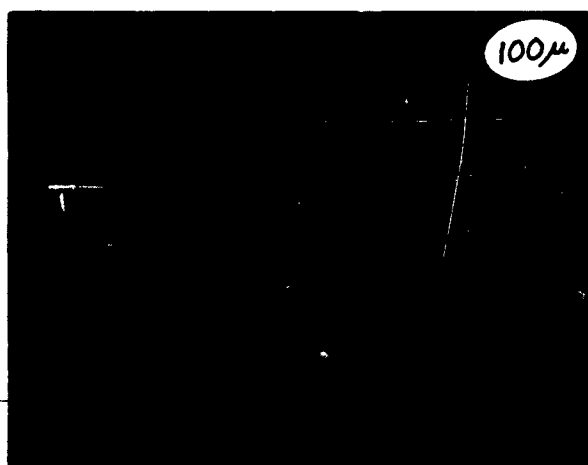
- (1) passivated silicon surfaces do not exhibit unstable charging effects; on the contrary, micrographs of passivated surfaces have better signal-to-noise ratios for a given recording time because of higher secondary emission from the passivated surface.



(a) No applied bias



(b) Emitter-base junction
reverse-bias = 2 v.



(c) Emitter-base junction
reverse-bias = 4 v.



(d) SiO₂ passivation removed.
Emitter-base junction
reverse-bias = 4 v.

Fig. 11 Power transistor section of WML105
functional electronic block

(ii) when no bias is applied, there is often a difference in contrast on opposite sides of a p-n junction covered with silicon dioxide; to date, no contrast difference has been observed on opposite sides of an unbiased bare silicon p-n junction.

(iii) a change in the contrast between the opposite sides of a p-n junction is produced when a reverse bias is applied, whether the junction is passivated, or is bare of oxide.

Furthermore, the contrast between opposite sides of a passivated p-n junction with no applied bias is believed due to variations in the oxide thickness. This hypothesis is now being checked out.

The above experimental observations imply that the passivating oxide layer does not act as an insulator under bombardment by the electron beam. This statement is consistent with known facts about electron bombardment induced conductivity.² As primary electrons (of approximately 15 kev energy, as used in these micrographs) lose energy in the insulator, they create many hole-electron pairs, which are mobile and neutralize any fields existing in the insulator. Thus, from this rather naive point of view, the potential of the silicon dioxide is maintained at the same value as the silicon substrate it covers, since internal fields are shorted out by these generated carriers. Further experiments are planned to improve the understanding of this mechanism.

A Westinghouse silicon field-effect device was also examined in the scanning electron microscope to determine whether it was possible to locate the channel position under the evaporated gate electrode. (See Section B.3.,

2. K. G. McKay, "Electron Bombardment Conductivity in Diamond", Phys. Rev., 74, 1606 (1948).

below.) The geometry of the device is shown in Fig. 12. The source and drain regions are formed by diffusing a donor type impurity (phosphorous) into the p-type substrate. The channel is formed by a naturally occurring surface inversion layer at the silicon/silicon dioxide interface when the p-type material is of high specific resistivity. In the device examined, the channel length was 125 microns, the gate length was 175 microns, the thickness of the aluminum gate electrode was one micron, and the thickness of the silicon dioxide insulating layer was 0.4 micron.

The series of micrographs shown in Fig. 13 were obtained of this device to show the variations in surface potential at zero, 10 volts, 20 volts, and 30 volts bias. Here a 45° viewing angle was used, and thus the geometry of the device is foreshortened by 1.4142, as is shown by the ellipses (which represent circles in the plane of the device). In these micrographs the source electrode, the gate electrode, and the drain electrode of the left-hand device, and the source and gate electrodes of the right-hand device, were all grounded. A negative bias was applied to the substrate to back-bias the junctions. The parts of the surface which are at ground potential appear dark in the micrographs, while the parts affected by the bias appear light.

In Fig. 13(b) there is a dark diffuse area between the left-hand device and the edge of the silicon slice. This dark area is not present at the higher bias levels shown in Figs. 13(c) and 13(d). If the beam current in the microscope is reduced, then the extent of these dark regions is found to increase. It is suspected that these dark areas represent a non-uniform pinching off of the surface inversion layer. The disappearance of the dark area at higher bias potentials (or at increased electron beam currents) is

DWG. 625A889

THE GEOMETRY OF THE DEVICE

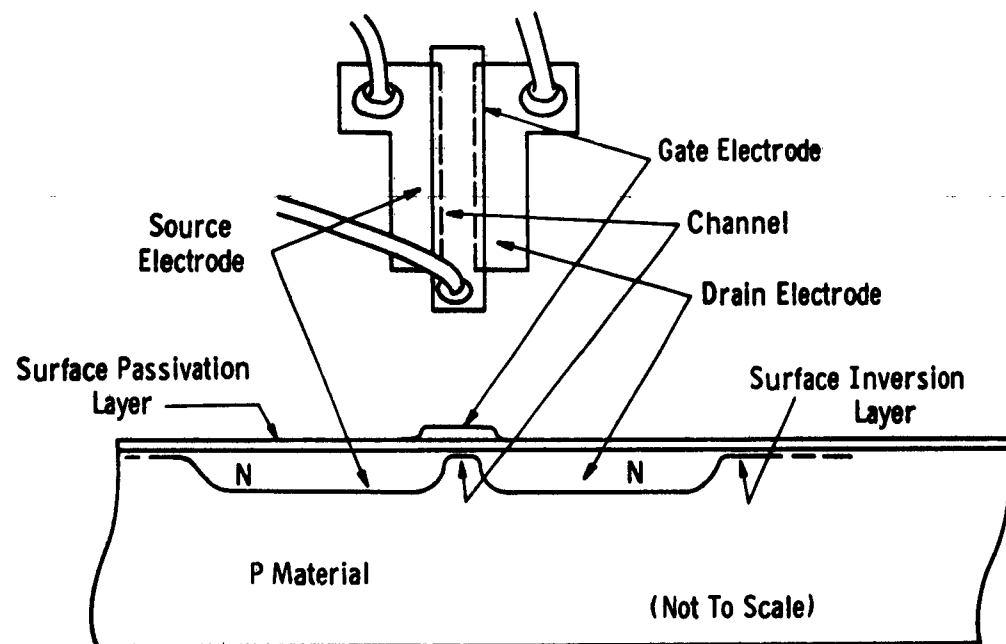
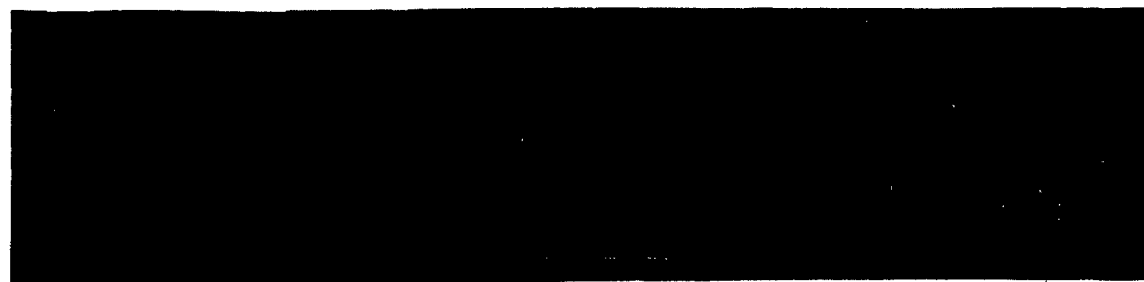


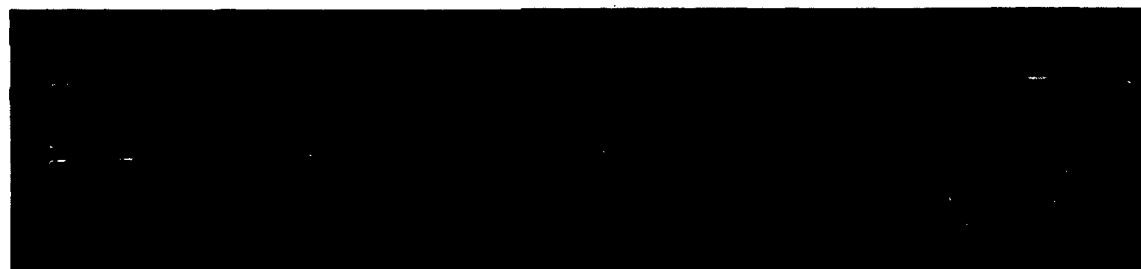
Fig. 12



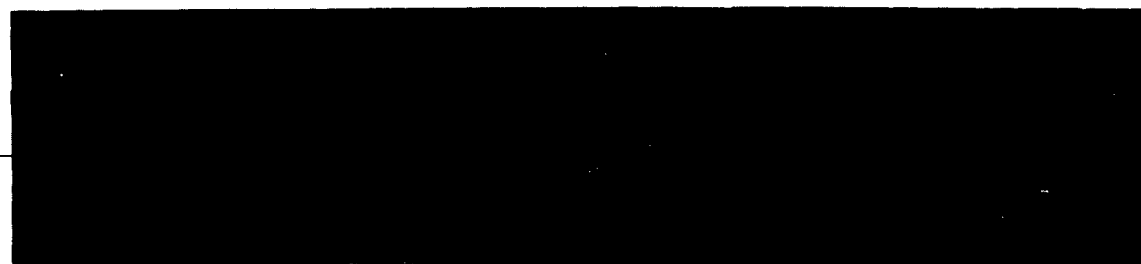
(a)



(b)



(c)



(d)

Fig. 13 - Scanning electron micrographs of a pair of silicon field-effect devices (a) with zero bias (b) with 10 volts bias (c) with 20 volts bias (d) with 30 volts bias

caused by an increased leakage current between this surface inversion layer and the substrate material, which causes in turn an increase in the tendency for the surface layer to pinch off. (The edges of the diffused source and drain regions are quite sharp, as can be seen by examining Fig. 15(b), in Section B.3., which is a micrograph of the same field-effect device at a higher magnification.)

In Figs. 13(b), 13(c), and 13(d), the presence of dark filaments is noticable. On both sides of these filaments lie diffuse dark areas, identified as non-uniformities in the surface inversion layers. It is considered that these dark filaments are caused by defects, or damage to the oxide layer prior to the diffusion step in fabrication, which allow the donor impurities to diffuse in along the lines indicated by the filaments.

B.3. Electron Beam Fabricating Techniques

One of the problems encountered in using electron beam techniques in the fabrication of semiconductor devices is that of registration. Specimens which are treated in the electron beam instrument, are often removed for various processing steps, and are then replaced in the instrument for additional treatment with the electron beam. Such procedures necessitate very accurate registration of the specimen when it is placed in the instrument. As a result, some effort has been devoted to investigating the factors affecting the ability of the electron beam apparatus to locate index marks on a specimen, where the beam impinges on the sample at normal incidence, and where the specimen is coated with a 0.5 micron layer of Kodak Photo Resist (KPR).

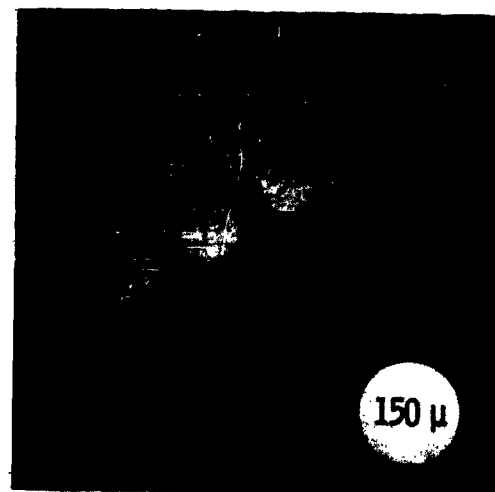
The sample used was a glass plate, partially covered with a 0.1 micron thick evaporated pattern of copper and aluminum. A detector that could be made sensitive to either back-scattered electrons alone, or to both back-scattered and secondary electrons, was placed within a few millimeters of the sample. Incident electron energies of 5 kev to 16 kev were used. Studies made prior to the period of the contract (O. C. Wells, PhD Dissertation, University of Cambridge, 1958) had indicated that in the case of a specimen that was not covered with KPR, it was possible to detect the differences in the material of the sample if the back-scattered electrons were collected, but not if only the secondary electrons were used.

It has been found that a different situation exists in this case, depending on whether or not the electron range was long enough to make the double trip through the KPR layer. At 16 kev energy, when the range of the electrons in the KPR (about 2 microns) was greater than twice the KPR thickness (1 micron), the boundaries between the glass and the metals, and between the metals themselves, could be clearly detected using the back-scattered electrons alone. But if the energy was reduced to 5 kev (as would be required to expose an image in the KPR with the best possible resolution), the image obtained using the back-scattered electrons no longer showed the boundaries through the KPR. At lower energy the boundary between the metal and glass underneath the KPR could be seen clearly, utilizing the low-energy secondary electron collection.

These effects are illustrated in Fig. 14. The test slide used for these micrographs consisted of circular spots of copper evaporated onto a non-conducting glass plate. These spots were then partially covered with a 0.1 micron evaporated aluminum layer. The entire plate was then coated with a 0.5 micron layer of KPR.



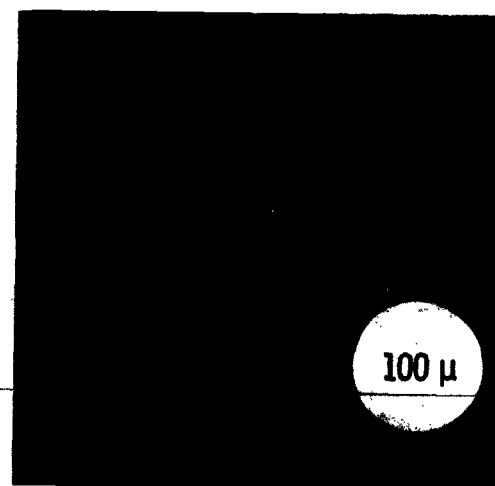
(a)



(b)



(c)



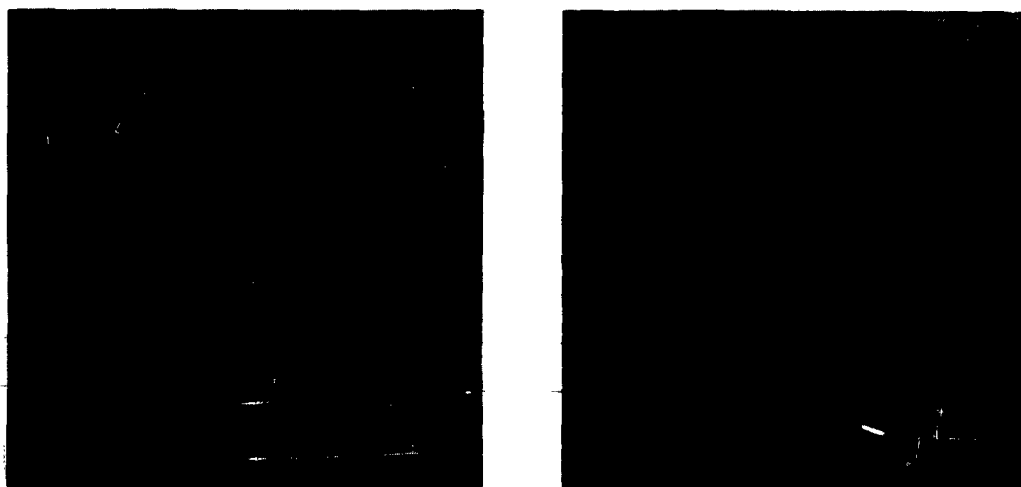
(d)

Fig. 14 - Scanning electron micrographs of glass test plate with copper spot pattern partially coated with aluminum film. Entire plate coated with Kodak Photo Resist layer. (a) low energy collection and 16 kev incident electrons ; (b) detector not sensitive to low energy electrons; (c) low energy collection and 5.5 kev incident electrons; (d) optical micrograph of test plate

In Fig. 14(a) the image shown was obtained using 16 kev incident electrons and the detector sensitive to low energy electrons. The bright areas produced by the charging of the non-conducting areas are noticable. In Fig. 14(b), when a detector was used that was not sensitive to low energy electrons, these charging effects do not produce any such bright regions in the micrographs, and the location of the edge of the conducting region is more difficult. This process is taken to its conclusion in Fig. 14(c), obtained using low-energy collection and 5.1/2 kev incident electron energies. Here the boundary may still be detected, even though the incident electron energy is insufficient to enable the double journey through the KPR. Figure 14(d) is an optical micrograph of the test plate, shown for comparison.

It was concluded, therefore, that for the purpose of locating an index mark, which could be a grounded evaporated metal strip on a non-conducting substrate, where the entire specimen is covered with a layer of KPR, the index strip may be located even when the electron range is of the same order as the KPR thickness.

The location of the channel position and width under the gate electrode of an insulated gate field-effect device is illustrated in Fig. 15. In Fig. 15(a) is shown a micrograph of the device with the source and drain regions back-biased in relation to the overlying gate electrode, which is held at the same potential as the substrate. The edges of the source and drain regions, as revealed by the potential distribution across the specimen surface, are seen to be diffuse, due to non-uniformities in the surface inversion layer. In Fig. 15(b) the same area is shown except that the current picked up by the back-biased p-n junctions in the work piece (due to the



(a)

(b)

Fig. 15 - Scanning electron micrographs (a) of a silicon field-effect device back-biased at 10 volts; and (b) as (a) but with the current waveform from the back-biased junction mixed into the video waveform, to reveal the position of the p-n junction under the aluminum gate electrode

impinging electron beam) is mixed with the video signal to give a composite effect, in which the positions of the junctions can be clearly seen. Thus the positions of the source and drain junctions defining the channel are revealed, even though they are covered with a 0.4 micron layer of silicon dioxide and a 1.0 micron aluminum layer.

B.4. Electron Beam Exposure of Resist Films

B.4.1. Uniform Film Thicknesses

The thickness of a resist film that is to be exposed to photons or electrons is an important parameter in determining how well the film meets the requirements of resolution and acid resistance. These are opposing requirements which must be optimized. To achieve the most effective protection of the substrate, the film must be thick enough so that no pores or thin spots exist through which the etchant can attack the substrate. Conversely, thicker films give rise to scattering effects which adversely affect the resolution. Figure 16 illustrates scattering as it occurs when a mask is used to limit the area of exposure using a flood electron beam. Scanning with a very narrowly defined electron beam would suffer a similar loss of resolution if the resist film were too thick.

Spinning the specimen on a centrifuge is an excellent method of obtaining uniform film thicknesses. For a given dilution of resist solution, the dry film thickness over a large area of the specimen appears to depend only on the angular velocity used during the spinning operation. Figures 17 and 18 show log-log plots of the dry film thicknesses of Kodak Photo Resist (KPR) and Kodak Metal Etch Resist (KMER)

DWG. 626A043

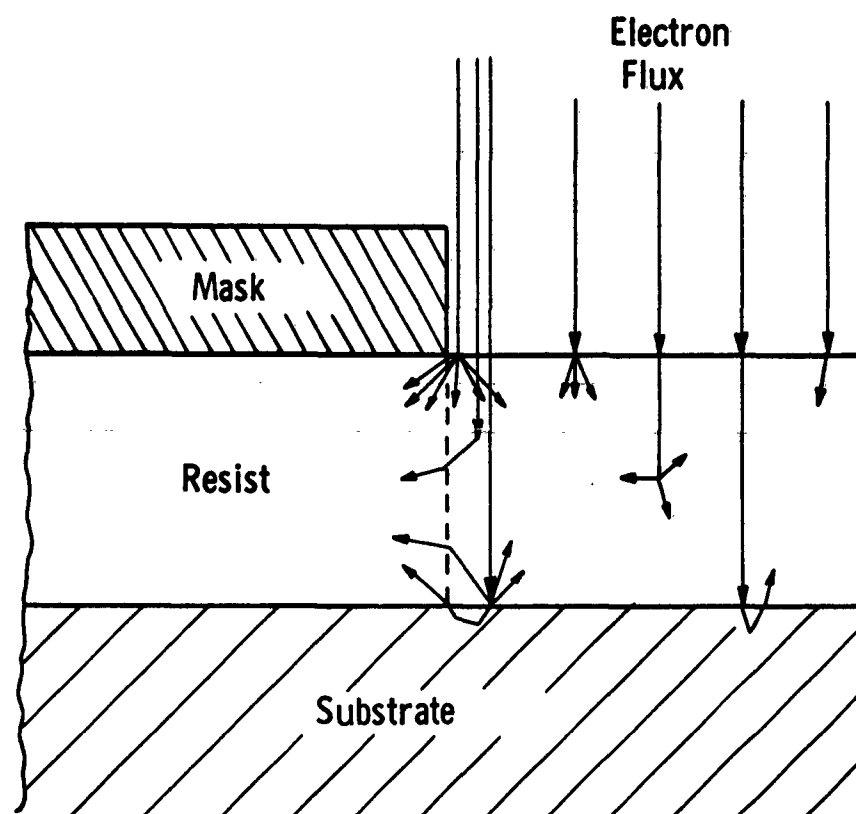


Fig. 16—Effect of scattering on resist film exposure

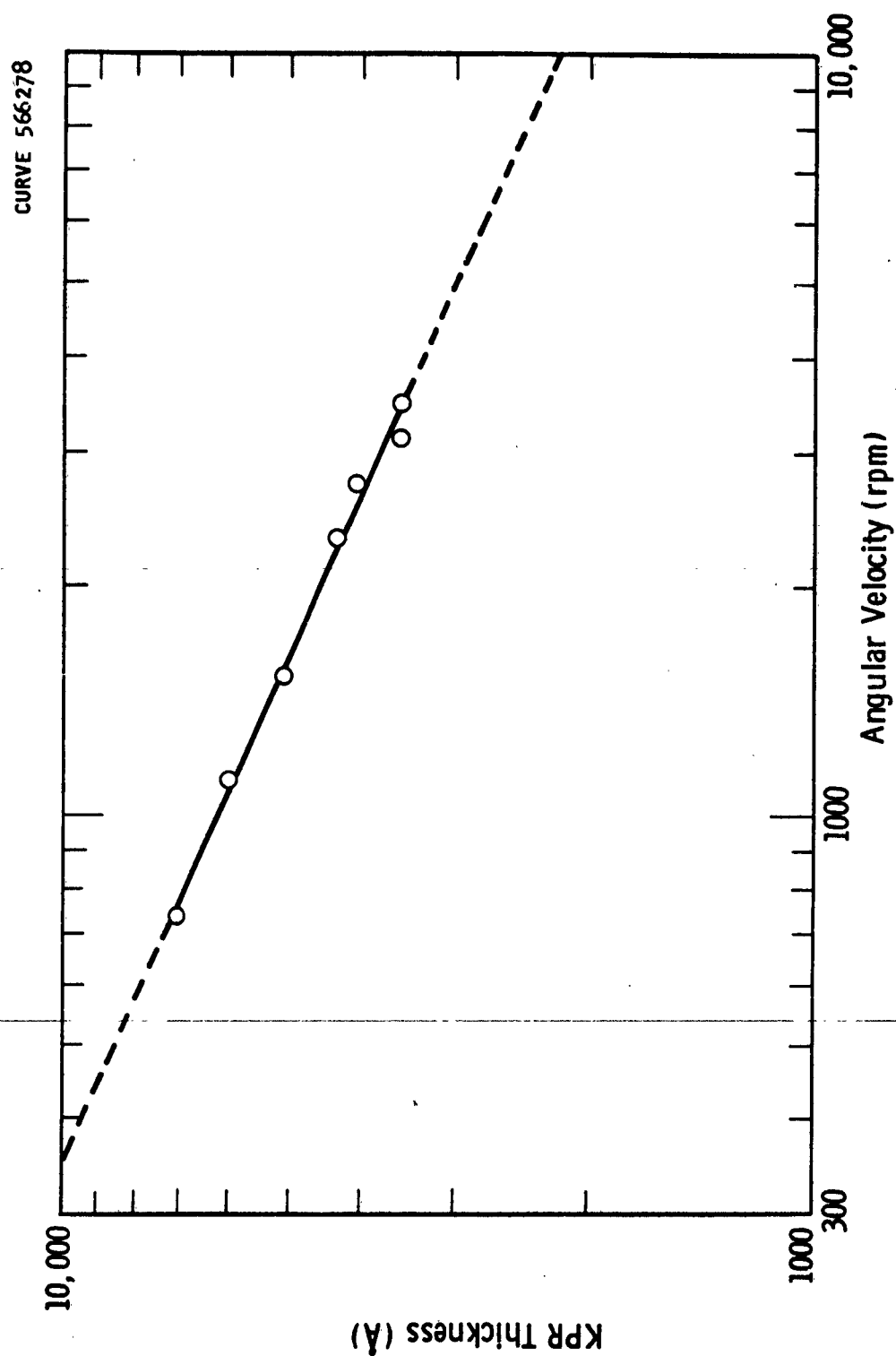


Fig. 17 --Variation of kodak photo resist thickness with angular velocity

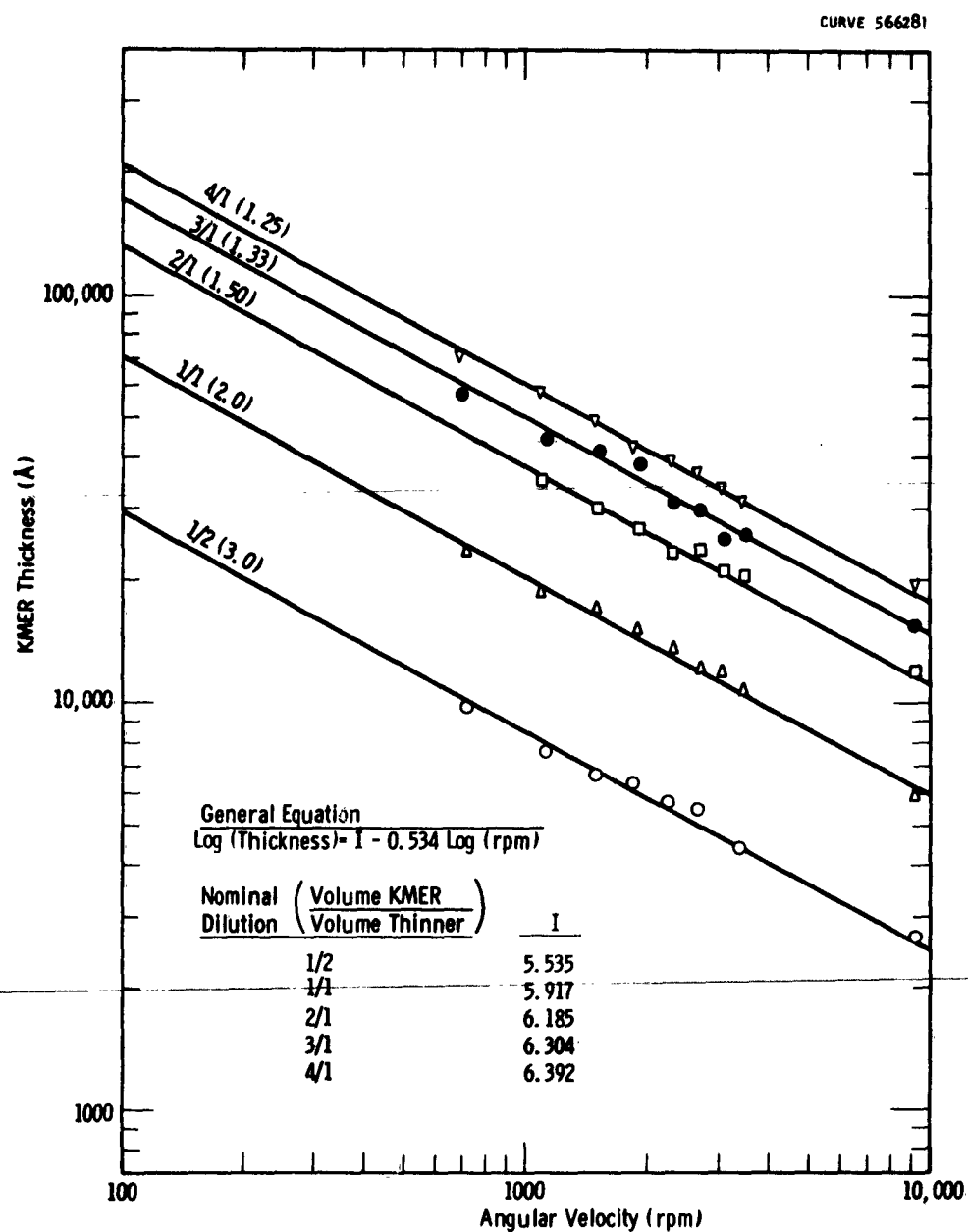


Fig. 18—Variation of kodak metal etch resist thickness with angular velocity

as functions of the angular velocity during spinning. Least square calculations were made to obtain straight line fits for the observed points. In the case of the KMER, the slopes of the lines were grouped so that the use of an average slope for all of the lines seemed reasonable. The line to fit the points for any dilution was obtained by calculating an intercept, I, for each point, using the equation:

$$\text{Log (thickness)} = I - M \text{ Log (angular velocity)}$$

where M is the average slope mentioned above. These intercepts are then averaged to obtain the equation of the line.

The average intercepts for the various dilutions are plotted in log-log form in Fig. 19 as a function of the dilution ratio, where the dilution ratio is given by:

$$\text{Dilution Ratio} = \frac{\text{Volume KMER} + \text{Volume Thinner}}{\text{Volume KMER}}$$

In Fig. 18, these dilution ratios are given for each line. The straight line obtained in Fig. 19 indicates that a predictable change in properties occurs for different dilutions of the same batch of KMER, and that, given the intercepts of two or more dilutions of the same batch of KMER, a dilution ratio can be calculated to give a specified film thickness for a specified angular velocity.

Specimens from different batches of KMER cannot be used with such calculations since KMER properties vary greatly from batch to batch. Thus it is necessary to perform calibration tests with each batch used. Table I gives the thicknesses obtained at 3500 rpm for specimens of four batches of undiluted KMER, and shows this high degree of variability.

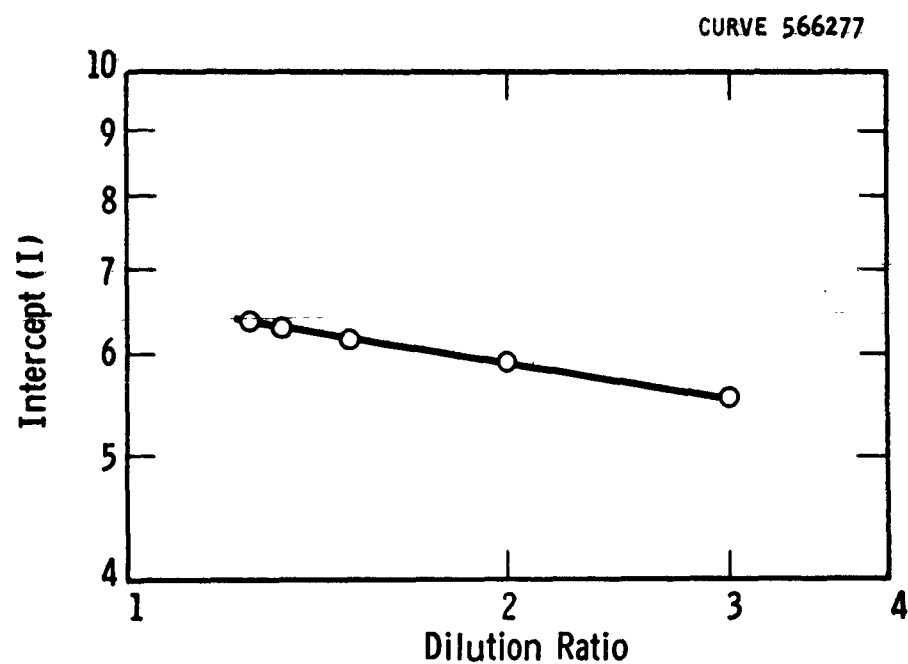


Fig. 19—Intercepts of KMER dilution curves vs.
dilution ratio, $\frac{\text{Volume KMER} + \text{Volume Thinner}}{\text{Volume KMER}}$

Table I

Dry Film Thickness (KMER)

(All spun at 3500 rpm)

| <u>Batch Number</u> | <u>Thickness (microns)</u> |
|---------------------|----------------------------|
| 6201 | 8.1 |
| 6208 | 4.6 |
| 6209 | 6.0 |
| 6213 | 6.5 |

The thickness measurements for this work were made using a Zeiss interference microscope and standard techniques. To reduce the possible introduction of error by variations in reflectivity, all samples were evaporated with an aluminum film prior to measurement. The thickness step for the measurements of Figs. 17 and 18 was made by scraping the resist from the substrate with a sharp blade.

B.4.2. Types of Organic Resists

Photosensitive organic resists fall into two categories, namely negative-acting and positive-acting. These designations are arbitrary, and follow the example of photographic emulsions, i.e. negative-acting resists become insoluble in the developer under the action of light or electron bombardment (analogous to the formation of insoluble silver deposits during the exposure of photographic emulsions). Conversely, positive-acting resists are insoluble in the developer, and the action of light, or electron bombardment, is to cause them to become soluble.

Patterns are produced in negative-acting resists by the cross-polymerization induced by light (or electron beams). Reactive sites exist in the polymer chains which, when activated, will form chemical bonds between the polymer molecules. This cross-polymerization forms molecules of a higher molecular weight than the polymer molecules in the unexposed dried film, and the cross-polymerized molecules are insoluble in the developing reagent. Treatment with this reagent removes all of the resist layer except the regions which were exposed. Examples of such resists are KPR, KMER, and dichromate-tanned polymers.

In the case of the positive-acting films, the resist is applied as a film that is insoluble in the developing reagent. The action of light or electron bombardment is to de-polymerize the material, causing the resist to become soluble in the developer. Patterns are produced by dissolving away the exposed areas. An example of a positive-acting resist is a material called Positop.

Positive-acting resist films should have somewhat better resolution than negative-acting resist layers, since the scattering effects during exposure will affect the layer in the region away from the substrate and will not distort a pattern from a mask or a narrow electron beam. This scattering effect is described in greater detail in Section B.4.3. below. It has been found that for a Positop film of approximately one micron thickness, the resolution obtained was better than the limit of the available resolution mask used during the exposure, i.e. better than 228 lines per millimeter. The best resolution obtained using KPR, which has the best resolution of all the Kodak resists, was less than 228 lines per millimeter for a resist layer of only 0.4 micron or less.

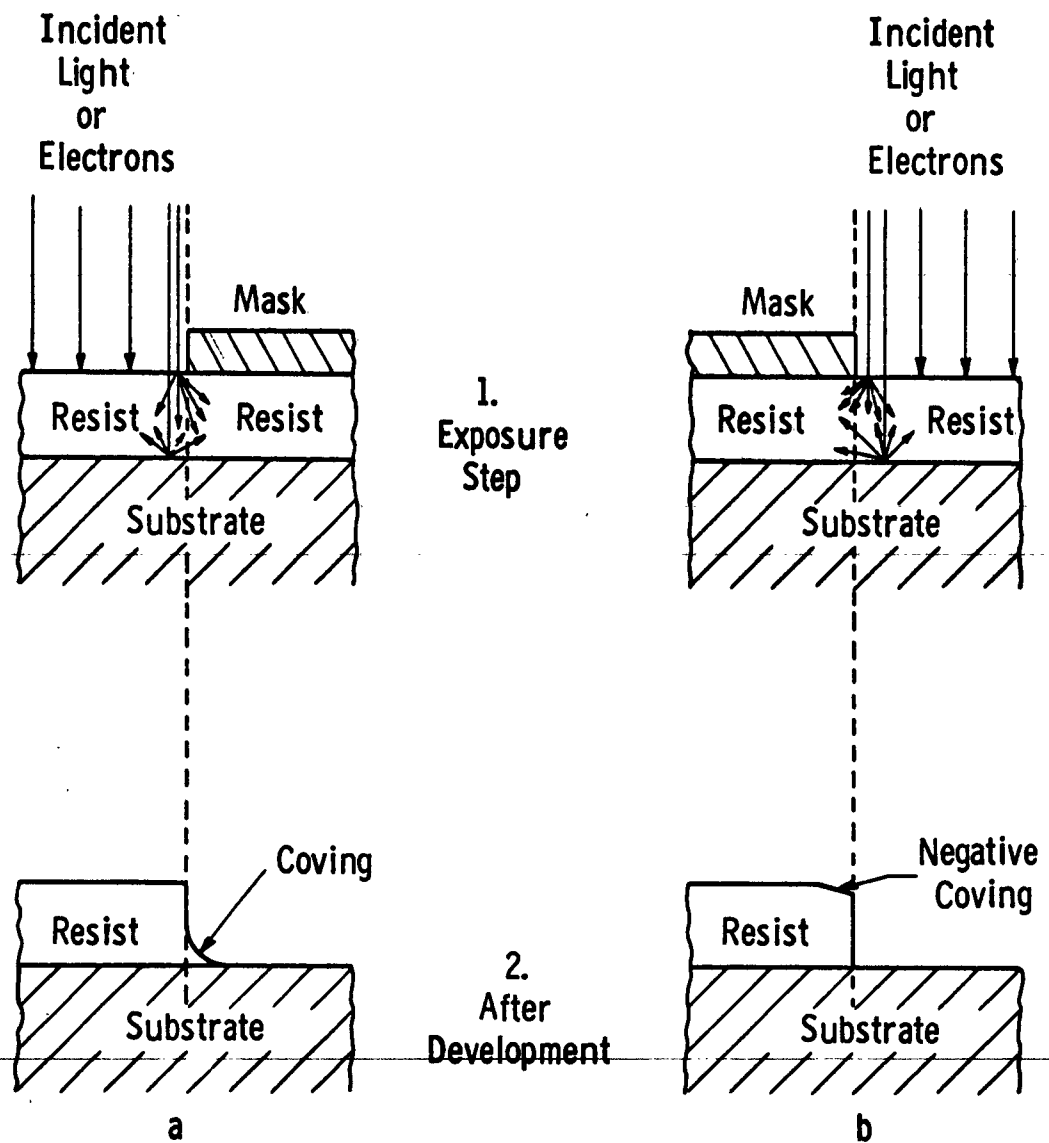
Positop, since it is impervious to the action of the developer (in fact it is not even wet by the developer), does not swell during development, and thus gives greater image stability than the negative-acting resists. KPR and KMER, on the other hand, absorb some of the developing solvent during the development step, and thus swelling occurs. Post-development baking will tend to drive the developer out of the film, but the subsequent shrinking does not appear to restore the film to the exact state it was in prior to development. An additional advantage of using Positop is that new patterns may be exposed in areas not exposed during earlier steps, thus making possible several sequential steps.

B.4.3. Problems in Using Resist Films

The scattering of photons or electrons which occurs during the exposure of resist films is the source of an effect known as "coving". Photons or electrons that are scattered into the resist under the mask will cause the formation of some insoluble material there when using negative-acting resist films. Since the development process will not remove this insoluble material, it remains behind and distorts the pattern of the mask. Figure 20(a) illustrates this situation, and shows the location where the coving occurs. Step 1., in the sketch, shows the action taking place during the exposure, and Step 2. shows the cross-section after development.

The situation existing when scattering occurs while using a positive-acting resist is sketched in Fig. 20(b). The scattered photons or electrons again cause partial exposure in behind the edge of the mask. The partially exposed material leaches out of the unexposed resist under the action of the developer, resulting in a somewhat thinner

DWG. 626A040



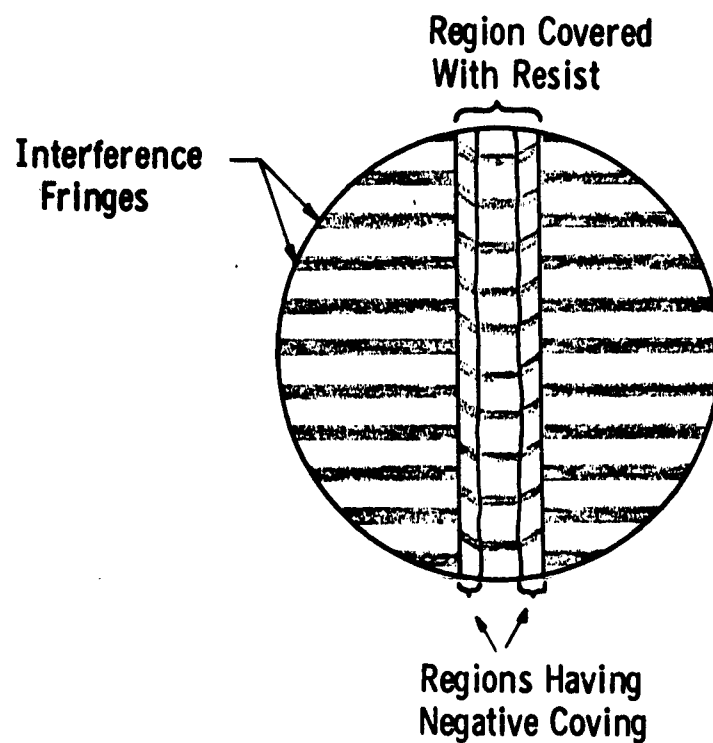
- a. Coving With Negative-Acting Resists
b. Coving With Positive-Acting Resists

Fig. 20

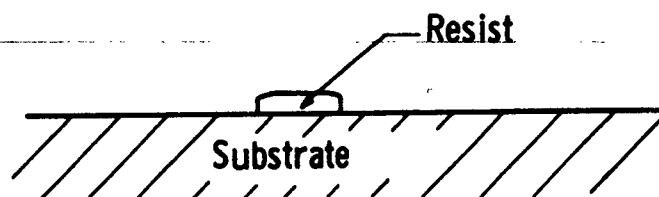
coating at the edge of the pattern. In this case, however, the area not covered by the mask receives a much greater exposure than that affected only by scattered photons or electrons. Thus the area not covered by resist after development is very nearly the same as the area defined by the mask. It should be noted that coving due to scattering may also occur when using very narrowly defined electron beams, as well as when using masks and flood beams.

The diagrams in Fig. 21 show an experimentally observed effect of coving on a positive-acting resist film after exposure to a flood electron beam. The scattering effect was increased by using a 0.005" wire as a mask with the wire touching the surface of the resist. The round cross-section of the wire allowed electrons to be scattered behind it. Measurement of the fringe displacements sketched in Fig. 21(a) indicate a total film thickness of 1.2 micron in the area not affected by the coving. At the edges, where the negative coving was at a maximum, the film appears to be about 0.9 micron thick. It should be noted that the outline of the wire is still well defined in the resist. Pattern distortion is generally less and resolution more satisfactory for the positive-acting resists than for the negative-acting films.

Dust is an obvious problem in the use of resist layers. Small dust particles may be capable of blocking off the photons or electrons during exposure. For negative-acting resists the problem becomes serious, as the result is a small pin-hole in the film, through which the etchant may attack the substrate. In the case of the



a. Interference Fringe Pattern



b. Cross Section of Resist Stripe
(Vertical Dimension Greatly Exaggerated)

Fig. 21

positive-acting resists, dust is not such a problem, as the result would be a small patch of resist left in an area where the resist had been removed. Such small regions are generally mechanically washed away during the etching operation.

B.4.4. Exposure Studies

Since KPR and KMER are the most commonly used photo-resist materials in semiconductor device technology, they were chosen for the initial work with electron beam exposure. Also, since KPR had proven feasible for use with the electron beam exposure, it was chosen as the first to be studied in detail.

Due to the problem of coving, and since it was suspected that unlinked polymer molecules should be leached out of partially exposed resist during development, the measurement of film thickness appeared to be a good indicator as to the degree of exposure, especially when final film thickness is compared with initial film thickness prior to exposure. A relationship between the thickness of an exposed, developed film and the exposure to light (or an electron beam) has been established. This relationship is shown in Figs. 22, 23, and 24 and is significant in the regions where the film thickness increases with increasing exposure, prior to the point where "saturation" appears to occur.

The effects of electron exposure value (total number of incident electrons) and the electron accelerating voltage have been studied for two initial film thicknesses, 3600 AU and 6100 AU. The specimens were spun at the appropriate rpm and pre-baked at 80°C for 15 minutes. Patterns were exposed at various accelerating voltages,

CURVE 566279

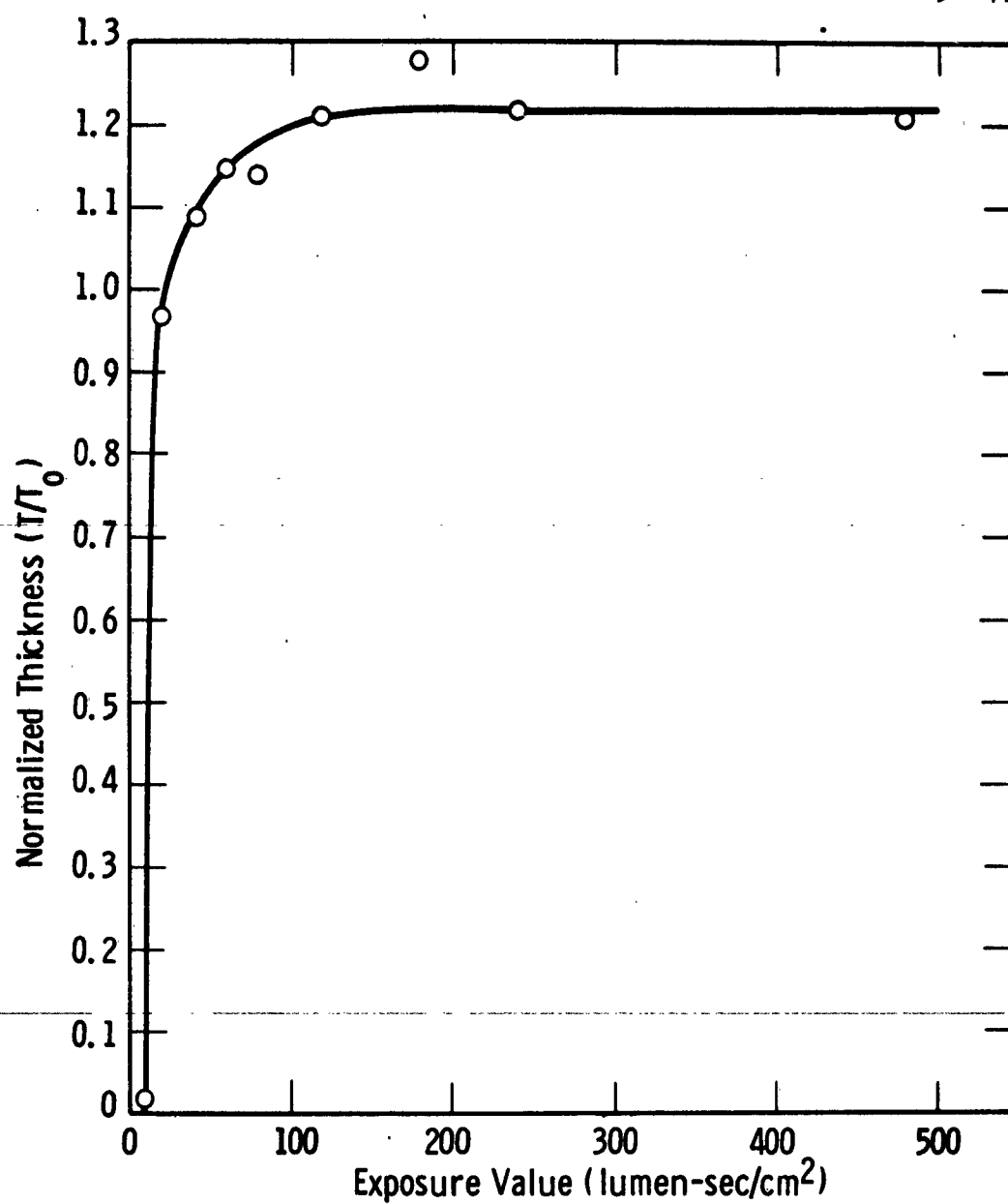


Fig. 22—Normalized KPR thickness vs. light exposure value
 $T_0 \sim 3600 \text{ \AA}$

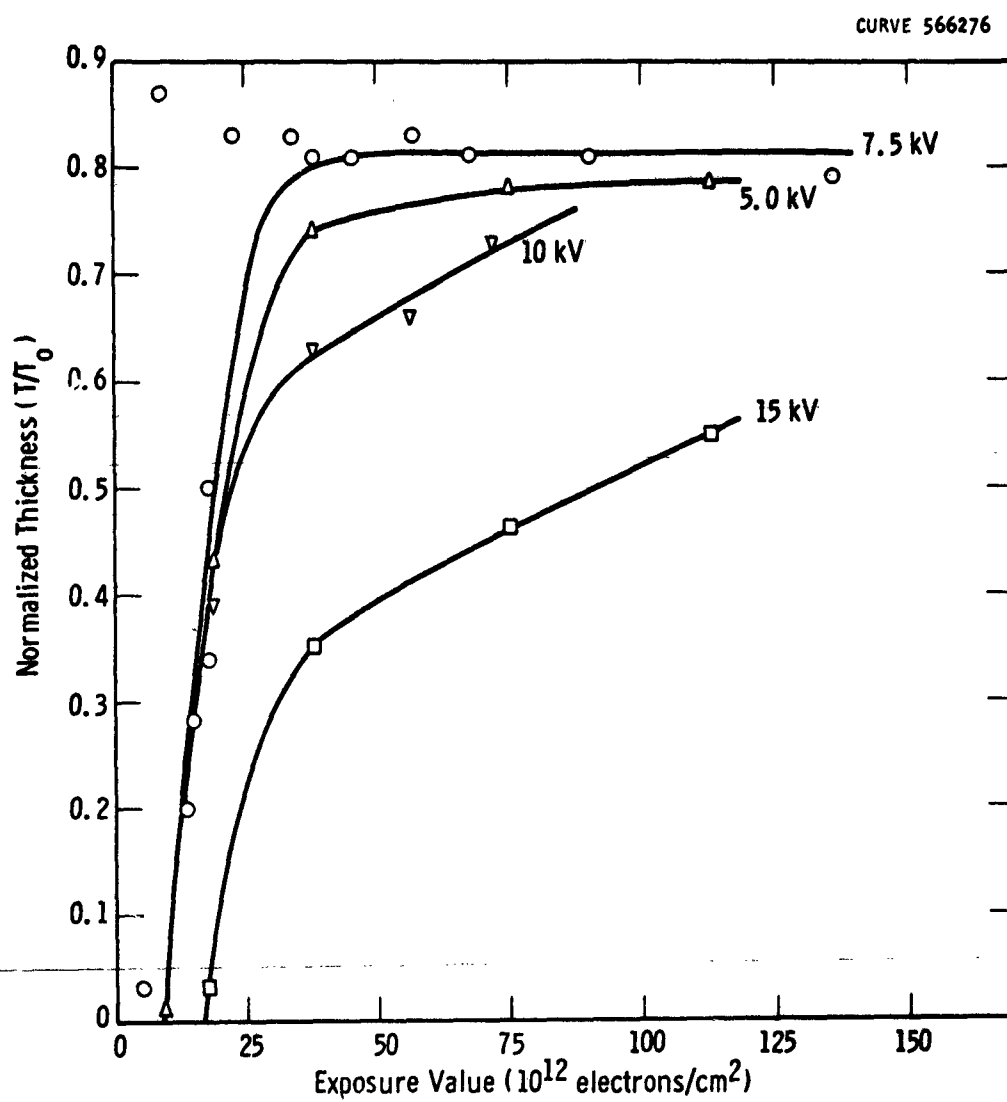


Fig. 23—Normalized KPR thickness vs. electron exposure value for 4 electron accelerating voltages, $T_0 \sim 3600 \text{ \AA}$

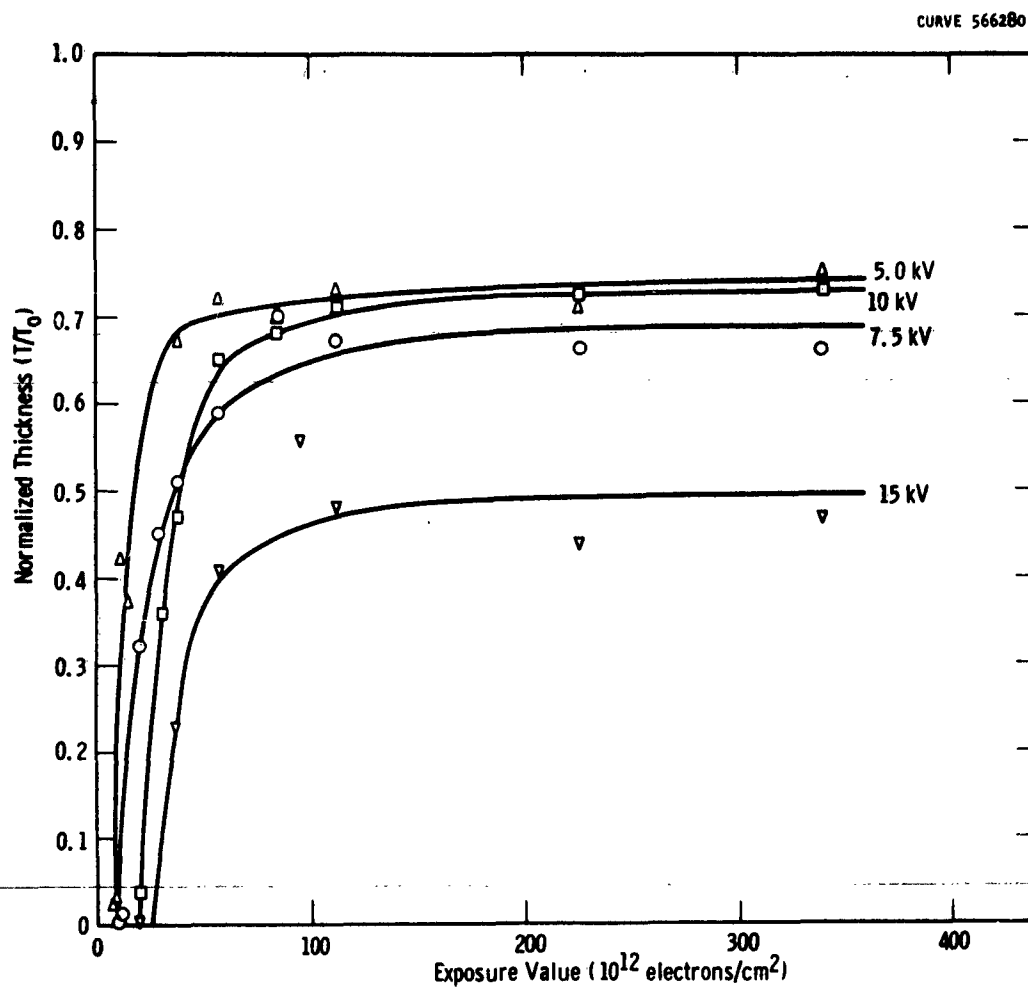


Fig. 24—Normalized KPR thickness vs. electron exposure value for 4 electron accelerating voltages, $T_0 \sim 6100 \text{ \AA}$

using appropriate current densities and times to obtain the desired exposure values. The films were then developed and post-baked at 220°C for 15 minutes. Thicknesses were then measured and compared to control samples.

Combinations of current density and time that result in the same exposure value have the same effect. A definite effect due to the accelerating voltage was found. Figures 23 and 24, in which T is the final exposed and developed thickness, and T_0 is the original film thickness, show that for a given T_0 , excessive accelerating voltage will tend to decrease the effectiveness of the electrons. For a T_0 of 3600 AU, 5.0 kv and 7.5 kv electrons were nearly alike in effect. 10.0 kv electrons were somewhat less effective, and 15.0 kv electrons much less. For an initial thickness of 6100 AU, 5.0 kv, 7.5 kv, and 10.0 kv electrons were about the same in their ability to expose the resist, while 15.0 kv electrons were still much less effecting. Thus it appears that for thicker films, electrons with higher energies become more effective. There also appears to be some minimum exposure value which must be exceeded before there is enough film remaining, after development, to detect.

C. Laser Techniques

C.1. Laser Bonding Gold Leads to Aluminum Coated Silicon

Gold wires have been attached to several specimens of aluminum coated silicon with negligible thermal damage. The elimination of the thermal damage that was prevalent in earlier samples is attributed to two factors: namely, higher quality evaporated aluminum films on the silicon substrates, and the adoption of two mil gold lead wires in place of the five mil wires used previously.

The higher reflectance of the better quality evaporated aluminum layers protects the silicon from absorbing very much energy from the portion of the laser beam that is not incident on the gold lead. Good quality, freshly evaporated aluminum films have a reflectance of about 90% at the 6940 AU wave length used, while poor quality, aged, aluminum films may have reflectances as low as 70%. Thus, much of the energy is reflected away from the silicon, when good quality, freshly evaporated, aluminum layers are used.

Reducing the wire diameter from five to two mils accomplished two things. It decreased the amount of gold that had to be heated by the laser beam, thus lowering the amount of energy needed. Also the contact is reduced in area, which also reduced the energy needed to affect a good bond. Since less energy is needed, the laser can be operated at a lower output, which will affect the silicon less where it is not covered by the gold lead.

The Trion LS-2 Optical Maser System was used in all present cases of lead attachment. The ruby laser rod used was a Trion 1/4-inch by 3-inch Total Internal Reflecting (TIR) rod. Cooling of the laser head was

accomplished by flowing liquid nitrogen up to a point just short of the head, where it was allowed to evaporate. The cold nitrogen gas was then allowed to flow into the head.

Figure 25 is a metallurgical section of Sample L-7, the first specimen made using the two mil gold wire. The gold wire was stretched horizontally across the substrate, and a point on the wire was located at the focal point of the laser beam. The laser burst was well enough controlled so that the wire was not severed during the bondings. One free end of the wire was broken off at the right-hand edge of the fused region. Note that there is still a small amount of thermal damage present. In this case the input energy to the laser head was 3400 joules. The sample was cross-sectioned nearly parallel to the axis of the gold wire.

Figure 26 is a metallographic section through Sample L-8, cross-sectioned at a 45° angle to the axis of the gold wire. Here there is slightly less depth of fusion into the substrate. Thermal damage appears to be very slight. For this bond the energy input to the laser head was 3330 joules. A gas bubble appears to have formed in the region where the gold was fused. This is possibly due to the volatilization of some material which is trapped by the gold during recrystallization. Figure 27 is a similar section through Sample L-10. Input energy to the laser head was 2995 joules for this case. Again the penetration into the substrate is small, and there is little evidence of thermal damage.

In order to test the strengths of these bonds, and to compare them with bonds made by the conventional thermocompression method. Three specimens were prepared with laser bonded leads, and three were prepared with thermocompression bonded leads. The wire used for all bonds was from the same

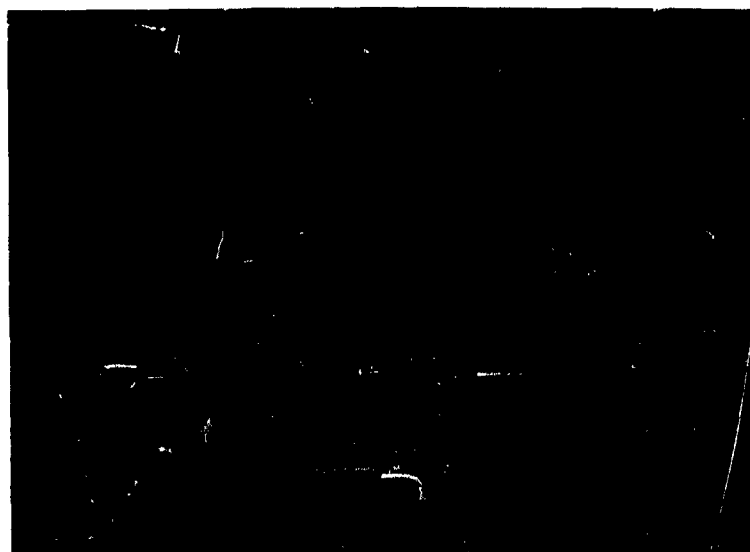


Fig. 25 Metallographic Section of Sample L-7, Two mil Gold Wire
Laser Bonded to Silicon Substrate (200 X)

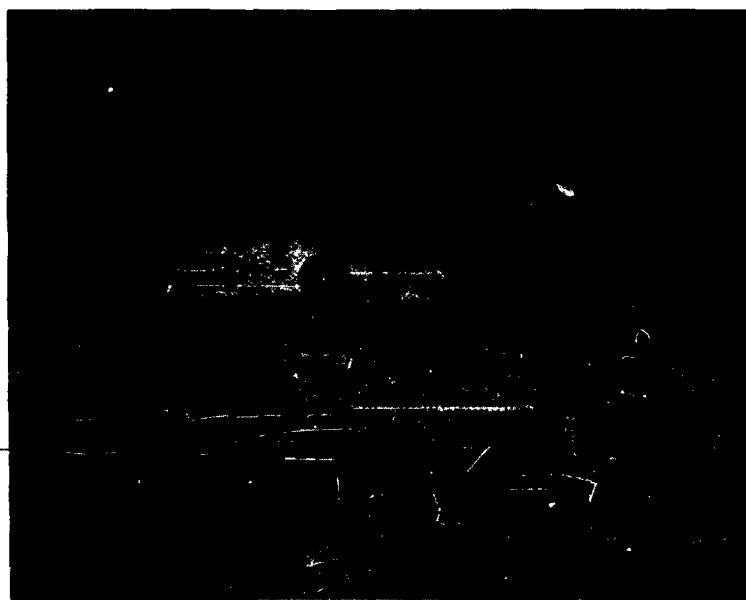


Fig. 26 Metallographic Section of Sample L-8, Two mil Gold Wire
Laser Bonded to Silicon Substrate (200 X)

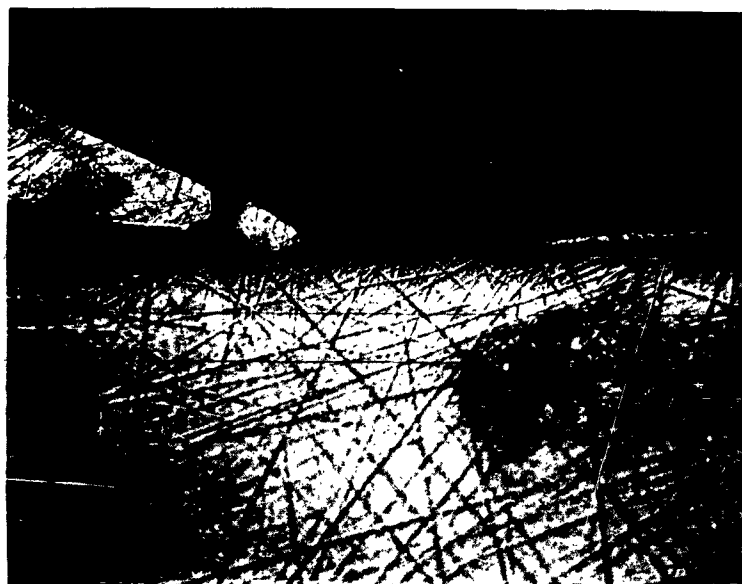


Fig. 27 Metallographic Section of Sample L-10, Two mil Gold Wire
Laser Bonded to Silicon Substrate (200 X)

spool. The wires were then bent at an angle of 45° to the substrate, as sketched in Fig. 28. The substrates were then cemented to a rigid support, and weights were hung from the wires, as shown in the sketch of Fig. 29. The weights were then increased until failure. The results of the tests are shown in Table II.

It should be noted that the laser bonded samples had about half the contact areas of the thermocompression bonded samples. While these tests seem to indicate greater strength for the laser bonds, since in no case did the lasered bond fail, it should be kept in mind that these tests are preliminary, and additional investigation will be necessary to obtain truly quantitative results.

C.2. Laser Bonding Gold Leads to Alloy Junction Diodes

Two types of silicon alloy junction diodes were obtained, one with gold-antimony alloyed into p-type silicon, the other with aluminum alloyed into n-type silicon. Contacts were already attached to the silicon chips of these diodes, but no leads were attached to the alloyed regions. The characteristics of these diodes were observed on an appropriate curve tracer. Laser Techniques were then used to attach two mil gold leads to the alloy pellet of each diode. The diode characteristics were again examined and found to be unchanged.

C.3. Laser Equipment - Neodymium Doped Glass Laser Rod

A neodymium doped glass laser rod was recieved and the output end coated with a 5% transmittance factor silver coating. Difficulties with the silver coating occurred due to the heating effects during use. A 4% transmittance factor dielectric film was then put on the rod in place of the

DWG. 626A042

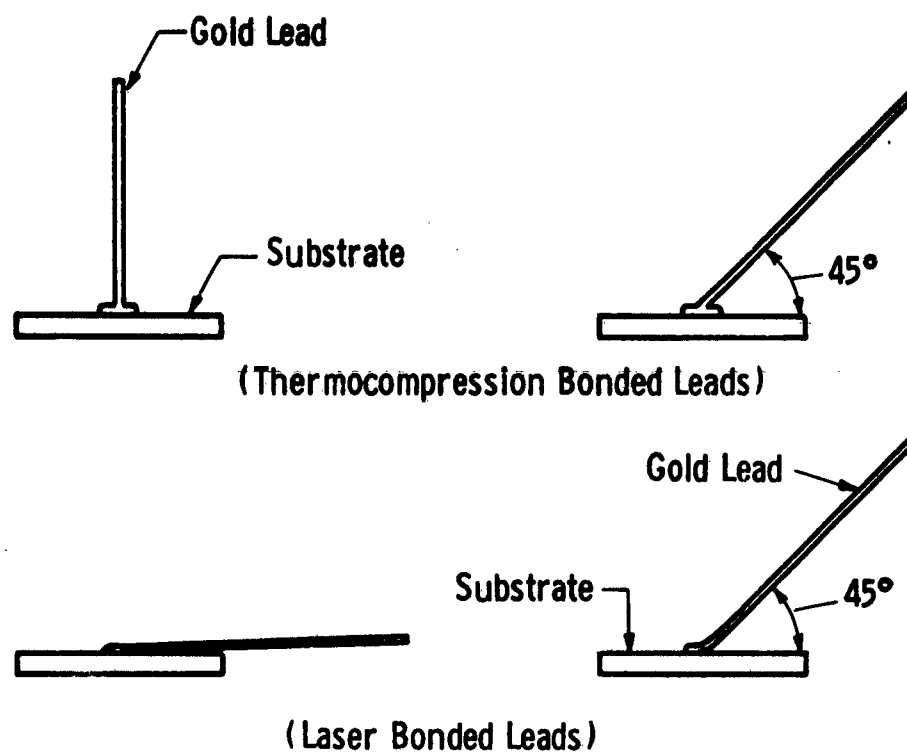


Fig. 28—Sketch of thermocompression bonded and laser bonded leads before and after bending, prior to testing

DWG. 626A041

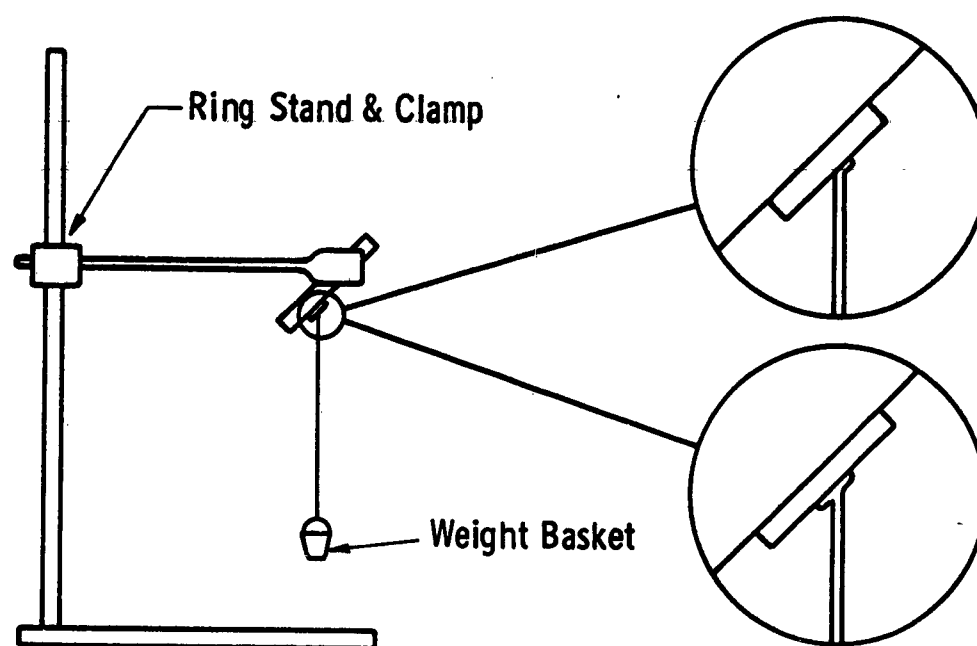


Fig. 29—Tensile/shear strength test, sketch of arrangement

Table II

Tensile/Shear/Bond Strengths

| <u>Method or Lead Attachment</u> | <u>Sample Number</u> | <u>Basket Weight at Failure</u> | <u>Point of Failure</u> |
|----------------------------------|----------------------|---------------------------------|-------------------------|
| Thermocompression Bonded | 1 | 27 gms | wire |
| Thermocompression Bonded | 2 | 11 | bond |
| Thermocompression Bonded | 3 | 19 | bond |
| Laser Bonded | 1 | 29 | wire |
| Laser Bonded | 2 | 30 | wire |
| Laser Bonded | 3 | 16* | wire |

* In this test the 16 gm weight was dropped giving an impact load.
Actual load at time of failure is unknown.

Table II

Tensile/Shear/Bond Strengths

| <u>Method or Lead Attachment</u> | <u>Sample Number</u> | <u>Basket Weight at Failure</u> | <u>Point of Failure</u> |
|----------------------------------|----------------------|---------------------------------|-------------------------|
| Thermocompression Bonded | 1 | 27 gms | wire |
| Thermocompression Bonded | 2 | 11 | bond |
| Thermocompression Bonded | 3 | 19 | bond |
| Laser Bonded | 1 | 29 | wire |
| Laser Bonded | 2 | 30 | wire |
| Laser Bonded | 3 | 16* | wire |

* In this test the 16 gm weight was dropped giving an impact load.
Actual load at time of failure is unknown.

silver. With the rod mounted in a cylindrical aluminized glass laser head, with a single linear xenon flash lamp, the rod had a firing threshold at room temperature of 150 joules input energy. With 330 joules input, the maximum output energy was only 0.05 joule.

Tests indicate that this rod requires excessively high input energies before laser action will occur. In the Trion laser head at least 2400 joules input was necessary for laser action. The maximum output energy that could be achieved with the Trion head was 0.174 joule for an input energy of 4556 joules. This low output, along with the fact that much of the output radiation is absorbed in the optics of the system (due to the characteristic wave length of this rod) has resulted in an inability to achieve laser bonds as yet. Modifications are now being made to the system to attempt to improve the performance.